ENGINEERING

Dual-modality photoacoustic and optical coherence tomography imaging simultaneously tracks transplanted stem cells and their viability

Sumin Park[1], Wei Qian[2], Jeff Folz[1], Van Phuc Nguyen[3], N. Dayanthi Perera[4], Wei Zhang[1], Abigail T. Fahim[4], Yannis M. Paulus[3]*, Xueding Wang[1]*

Copyright © 2026 The Authors, some rights reserved; exclusive licensee American Association for the Advancement of Science. No claim to original U.S. Government Works. Distributed under a Creative Commons Attribution License 4.0 (CC BY).

Monitoring transplanted cell viability in vivo, noninvasively remains a considerable challenge. By using multiwavelength photoacoustic microscopy powered by a reactive oxygen species (ROS)–responsive contrast agent, we can relatively and semiquantitatively assess and longitudinally monitor the viability of human-induced pluripotent stem cell–derived retinal pigment epithelium (hiPSC-RPE) cells in vivo. The contrast agent comprises colloidal chain-like gold nanoparticle (CGNP) clusters conjugated with IR775c, a heptamethine cyanine dye that undergoes selective oxidative quenching under elevated ROS conditions associated with cellular death (CGNP-IR775c). Dual-wavelength photoacoustic microscopy at 620 and 775 nanometers provides self-calibrated ratiometric measurements that enable relative viability assessment, distinguishing healthy from nonviable cell populations. In vitro studies demonstrated that CGNP-IR775c exhibited biocompatibility and showed dose-dependent ROS sensitivity across physiologically relevant H_2O_2 concentrations. hiPSC-RPE cells labeled by CGNP-IR775c were subretinally transplanted into living rabbit eyes and longitudinally monitored for 2 weeks, showing that laser-induced oxidative stress produced measurable photoacoustic signal changes that were consistent with the viability status of the transplanted cells. The imaging technology developed here provides a practical solution for noninvasive, longitudinal, and semiquantitative assessment of the transplanted cell viability in vivo, and may contribute to ophthalmology cell-based therapy in both preclinical and clinical settings.

INTRODUCTION

Age-related macular degeneration, retinitis pigmentosa, and related retinal degenerative diseases are leading causes of irreversible vision loss, affecting millions globally with limited treatment options (*1*). Stem cell–based therapies are emerging as a promising approach to addressing these previously untreatable diseases. Given that retinal tissues have limited regenerative capacity after damage, stem cell therapy has been attracting attention as a promising treatment, with numerous preliminary studies demonstrating its potential (*2*, *3*).

Despite nearly two decades of clinical research and encouraging preliminary results, widespread use of stem cell therapies for ocular diseases remains hampered by a fundamental challenge, which is our limited ability to monitor and understand the behavior and mechanisms of the transplanted cells after delivery. Clinical success depends on the survival of transplanted cells and, in many cases, on their structural integration into the host tissue (*4*–*6*), yet these aspects remain challenging for current monitoring technologies to evaluate reliably. Anoikis, mechanical stress, oxidative stress, and immune responses can lead to inhibited proliferation and differentiation, ultimately causing graft failure (*7*). In current practice, global anatomical imaging and functional assessment performed weeks to months after transplantation serve as the main indicators of successful treatment (*8*). These assessments fail to evaluate the location and survival of the transplanted cells in the critical early posttransplantation phase, when cellular fate is determined. Early monitoring of graft status could help inform timely clinical decisions. For example, immunosuppressive management has been shown to critically determine transplanted cell survival in subretinal transplantation models (*9*). Yet current technologies do not provide the real-time cellular information needed to guide such interventions. This gap between dynamic cellular responses and our ability to track and monitor them in real time represents one of the main obstacles to advancing regenerative medicine.

Each of the imaging modalities in use for stem cell tracking has considerable limitations that prevent widespread clinical translation. Superparamagnetic iron oxide nanoparticle-based magnetic resonance imaging offers good anatomical localization, but it is unable to differentiate between living and dead cells since the contrast remains the same regardless of the cellular fate. Although positron emission tomography and single photon emission computed tomography have great sensitivity, their applicability for longitudinal monitoring is limited due to the short half-lives of commonly used radioisotopes, their complex radiochemistry, and ionizing radiation dose requirements and safety considerations. Furthermore, bioluminescence and fluorescence imaging need genetic modification of cells (*10*), which raises safety and regulatory concerns and makes them inadequate for clinical applications (*11*). Critically, none of these approaches can offer depth-resolved imaging, clinical safety profile, and molecular specificity needed for viability evaluation of transplanted cells. Innovative imaging tools that can provide quantitative, longitudinal assessment of transplanted cell viability without sacrificing clinical translatability or patient safety are needed in this field.

A possible technique for overcoming these challenges is photoacoustic microscopy (PAM) powered by nanoparticle contrast agents. As demonstrated by previous publications, PAM is capable of visualizing the structure and function of the retina and choroid of the eye noninvasively with micron-scale resolution (*12*–*14*). Our PAM system

[1]Department of Biomedical Engineering, University of Michigan, Ann Arbor, MI 48109, USA. [2]IMRA America, Inc., 1044 Woodridge Ave., Ann Arbor, MI 48105, USA. [3]Department of Ophthalmology, Department of Biomedical Engineering, Wilmer Eye Institute, Johns Hopkins University School of Medicine, Baltimore, MD 21287, USA. [4]Department of Ophthalmology and Visual Sciences, University of Michigan, Ann Arbor, MI 48105, USA.
*Corresponding author. Email: ypaulus1@jh.edu (Y.M.P.); xdwang@umich.edu (X.W.)

is capable of three-dimensional visualization in the eye using light fluence as low as 1% of the ANSI safety limit (*15*) and has been demonstrated to be safe in a safety evaluation (*16*). Photoacoustic (PA) imaging has previously been applied to stem cell tracking in ophthalmology: Gold nanosphere-labeled mesenchymal stem cells in the anterior segment were tracked using a combined ultrasound/PAM imaging platform, enabling real-time monitoring and spectroscopic distinction of labeled cells from background tissues (*17*); chain-like gold nanoparticle (CGNP)–labeled ARPE-19 progenitor cells in the subretinal space of rabbit eyes were tracked using combined PAM/optical coherence tomography (OCT)/fluorescence imaging system (*18*); and human-induced pluripotent stem cell–derived retinal pigment epithelium (hiPSC-RPE) cells labeled with ultra-miniature CGNP clusters were imaged in vivo using combined PAM/OCT/fluorescence imaging (*19*). However, these approaches were limited to anatomical localization of transplanted cells and were not capable of reporting cell viability, as the contrast agents used provided static, reactive oxygen species (ROS)–unresponsive signals. Beyond cell tracking, PA imaging has also been explored for viability sensing through ROS-responsive contrast agents. For example, Dhada *et al.* (*20*) demonstrated in vivo PA monitoring of mesenchymal stem cell viability using a ROS-sensitive probe, establishing proof of concept for metabolic state reporting via PA signal changes. Despite this advance, such approaches have not been demonstrated in the subretinal space nor combined with a simultaneous cell localization modality in a ratiometric framework. The development of responsive PA contrast agents that can dynamically report cellular status is essential to using PAM for cell viability monitoring. In this regard, ROS are useful indicators since their elevated levels indicate cellular stress and apoptosis (*21*, *22*). Accumulation of ROS triggers a cascade of oxidative damage that occurs concurrently with disruption of the mitochondrial membrane (*23*, *24*), decreased esterase activity (*25*, *26*), increased caspase activation (*27*, *28*), and loss of membrane integrity (*29*, *30*), providing several complementary markers for assessing cell viability (*31*). Thus, this internal metabolic signal could be converted into measurable imaging signals by a ROS-responsive contrast agent, allowing for noninvasive, longitudinal monitoring of transplanted cell fate.

Here, we report the development of CGNP-IR775c, a dual-component PA contrast agent designed for semiquantitative, longitudinal monitoring of stem cell viability in vivo. The IR775c dye molecules producing ROS-responsive signals when excited at 775 nm are combined with CGNP clusters which provide persistent reference PA signals under 620-nm excitation for cell localization. Because elevated intracellular ROS levels during cellular death induce oxidative quenching of IR775c molecules as the predominant signal reduction mechanism, preferentially attenuating the PA signal amplitude at 775 nm relative to the ROS-insensitive reference PA signal amplitude at 620 nm from the CGNP clusters, the ratio of PA signal amplitudes acquired at 775 and 620 nm provides a self-calibrated metric for semiquantitative assessment of cell viability. This dual-wavelength ratiometric approach overcomes notable obstacles associated with single-wavelength imaging techniques, including variations in excitation laser fluence, contrast agent concentration, and imaging conditions, thereby enabling high robust and accurate longitudinal cell viability assessment. Through in vitro studies using ARPE-19 and hiPSC-RPE cells, as well as in vivo studies using transplanted hiPSC-RPE cells, we systematically characterized the physicochemical properties, ROS responsiveness, and biocompatibility of CGNP-IR775c. Our findings show that PAM powered by CGNP-IR775c can effectively distinguish viable from nonviable transplanted stem cells with high spatiotemporal resolution, demonstrating a platform that could transform our ability to monitor cell-based therapeutics and accelerate the clinical translation of regenerative medicine. Figure 1 shows the schematic illustration of CGNP-IR775c nanoplatform for ROS-responsive PA monitoring of transplanted hiPSC-RPE cell viability in vivo.

RESULTS

Design and physicochemical characterization of CGNP-IR775c

We designed CGNP-IR775c, a multifunctional PA contrast agent that includes (i) CGNP clusters for providing stable PA reference signals, (ii) polyethylene glycol (PEG) coating for enhanced colloidal stability and biocompatibility, (iii) RGD peptides for improved cellular targeting, and (iv) IR775c as a ROS-responsive heptamethine cyanine near-infrared (NIR) reporter (Fig. 2A). By combining ROS-responsive IR775c with the CGNP clusters that provide stable reference PA signals over the full duration of longitudinal imaging, our design addresses limitations of current contrast agents and allows assessment of transplanted cell viability through a ratiometric dual-wavelength PAM strategy.

Transmission electron microscopy (TEM) analysis confirmed that GNP monomers exhibited a uniform spherical morphology with an average diameter of 20.0 ± 0.9 nm (Fig. 2B). Following sequential functionalization with CALNN pentapeptides, cysteamine, PEG, RGD peptides, and IR775c, the assembled CGNP-IR775c maintained its characteristic chain-like architecture without aggregation, measuring 25.2 ± 1.5 nm in width and 76.2 ± 1.5 nm in length (Fig. 2C). The ideal size profile for ocular applications is less than 100 nm, which allows for penetration through the corneal and conjunctival barriers while avoiding rapid renal clearance (*32*–*35*).

Ultraviolet-visible (UV-Vis) spectroscopy of CGNP-IR775c revealed two distinct absorption peaks corresponding to the longitudinal surface plasmon resonance (SPR) of the CGNP clusters at 620 nm and the NIR absorption of IR775c at 775 nm (Fig. 2D). The chain-like architecture of CGNP-IR775c was confirmed by the red-shifted longitudinal SPR peak observed at 620 nm, compared to the localized SPR of spherical GNP monomers, which typically appears at about 520 nm. This red shift also indicates that the absorption peak of CGNP-IR775c falls outside the dominant hemoglobin absorption window, thereby minimizing spectral interference during in vivo PA imaging (*36*). In addition, the 775-nm peak arose from the extended π-conjugation of the heptamethine backbone, which enables electron delocalization across the molecule and results in the absorption in the NIR range (*37*). With a distinctive peak at mass/charge ratio (*m*/*z*) 553.30, mass spectrometry confirmed that the carboxylic acid successfully replaced the chlorine group in the IR775c structure (Fig. 2E) (*20*). Fluorescence spectroscopy revealed excitation at 750 nm and emission at 775 nm (Fig. 2F), which is appropriate for PA applications and comparable with the characteristics of heptamethine cyanine (*38*). The polymethine chain's susceptibility to ROS-induced quenching positions IR775c as a dynamic reporter of oxidative stress (*39*, *40*).

Zeta potential measurements revealed consistent negative surface charges ($\zeta = -39.63 \pm 0.95$ mV, $n = 3$) for CGNP-IR775c (Fig. 2G). The broad, multipeak distribution profile reflects the polydisperse

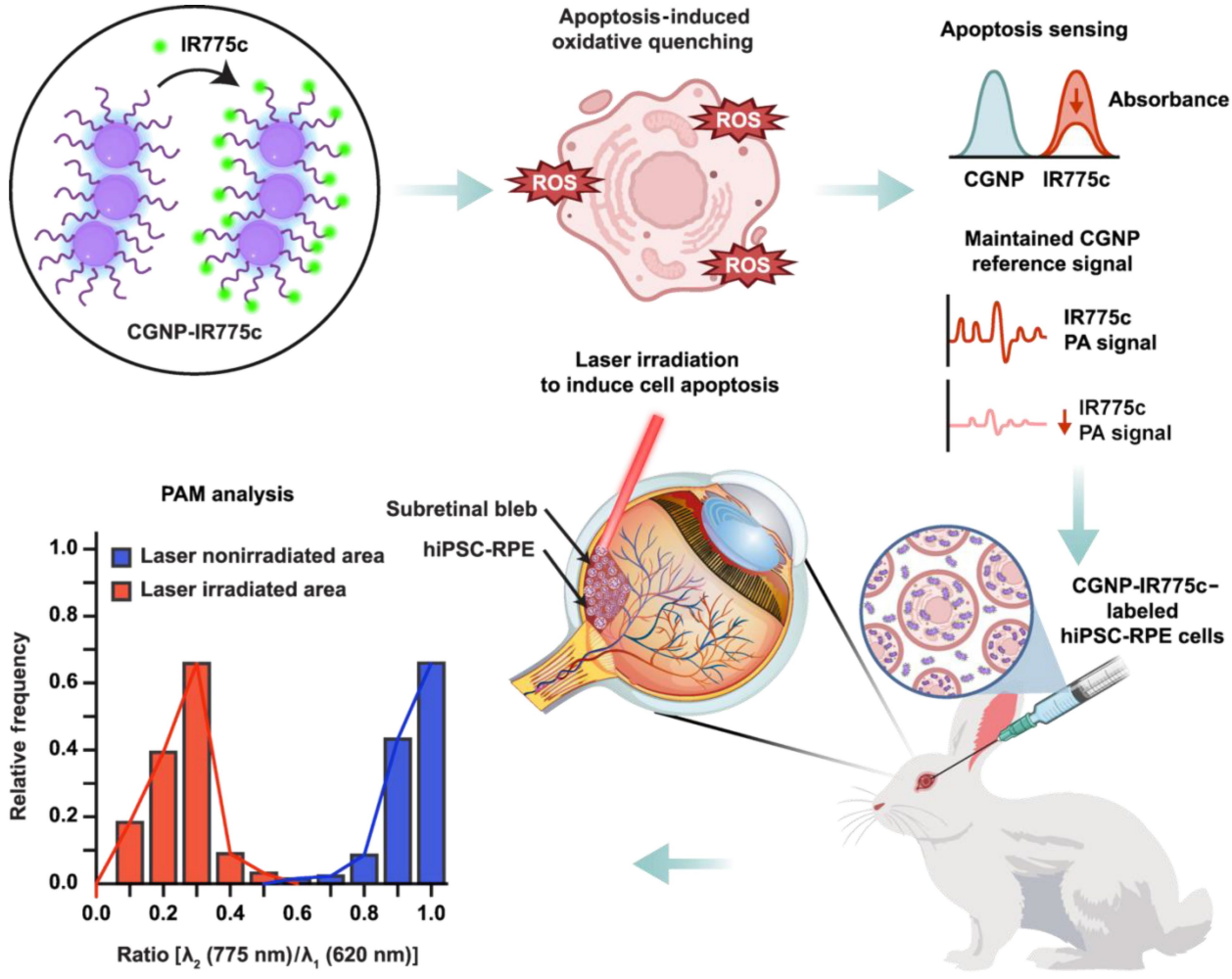

Fig. 1. Schematic illustration of CGNP-IR775c nanoplatform for ROS-responsive PA monitoring of transplanted hiPSC-RPE cell viability in vivo. The structural composition of CGNP-IR775c (top left) shows CGNP clusters (purple spheres) conjugated with IR775c dye molecules (green) and stabilized with polyethylene glycol (PEG) and RGD peptides for enhanced cellular uptake. Upon cellular stress (top middle), ROS generation leads to selective quenching of the IR775c while preserving CGNP structures. Differential optical and PA responses (top right) show maintained CGNP absorption at 620 nm serving as an internal reference, while IR775c absorption at 775 nm decreases upon ROS exposure, resulting in decreased PA signal amplitude. CGNP-IR775c–labeled hiPSC-RPE cells undergo subretinal transplantation into New Zealand white rabbit eyes via subretinal injection (bottom right). For cellular death induction, controlled laser irradiation induces localized oxidative stress in specific regions in the eye. Semiquantitative ratiometric PAM analysis (bottom left) comparing laser-irradiated versus nonirradiated regions demonstrates clear population separation, distinguishing healthy versus dead cells. Arrows indicate workflow progression from nanoparticle design through cellular labeling, transplantation, stress induction, and semiquantitative viability assessment after imaging. This integrated platform enables noninvasive, longitudinal monitoring of transplanted cell viability through dual-wavelength PAM. Figure partially created in BioRender. Park, S. (2026) https://BioRender.com/0l6zcto.

nature of the CGNP assemblies and the additional surface charge heterogeneity introduced by IR775c conjugation at varying densities across the nanoparticle surface, resulting in a distribution of electrophoretic mobilities (*41*–*44*). Although the difference in mean zeta potential between pure CGNPs and CGNP-IR775c is modest ($\Delta\zeta \approx 1.2$ mV), the notable broadening of the distribution profile and emergence of multipeak character following IR775c conjugation provide evidence of surface modification consistent with IR775c incorporation (fig. S2). The near-identical overlap of the three individual measurement traces confirms the high reproducibility of the zeta potential measurement, indicating robust colloidal stability and supporting the suitability of CGNP-IR775c for biomedical applications.

ROS-responsive optical and PA properties

The design and synthesis strategy of CGNP-IR775c was engineered to provide ROS-responsive imaging capability (Fig. 3A). Upon exposure to ROS, IR775c undergoes oxidative quenching, leading to diminished PA signals at 775 nm while the CGNP maintains its PA properties. The ROS-responsive behavior of CGNP-IR775c was investigated using spectroscopic and PA analyses to evaluate its potential as a dynamic contrast agent for monitoring oxidative stress and relevant cellular death. Since hydrogen peroxide (H_2O_2) is a key member of the ROS in oxidative stress, cellular apoptosis, and inflammation (*45*, *46*), we used it as a physiologically relevant oxidative stressor to evaluate the ROS responsiveness of CGNP-IR775c. UV-Vis spectroscopy revealed that exposure to 50, 100, 200, 300, and 500 μM H_2O_2

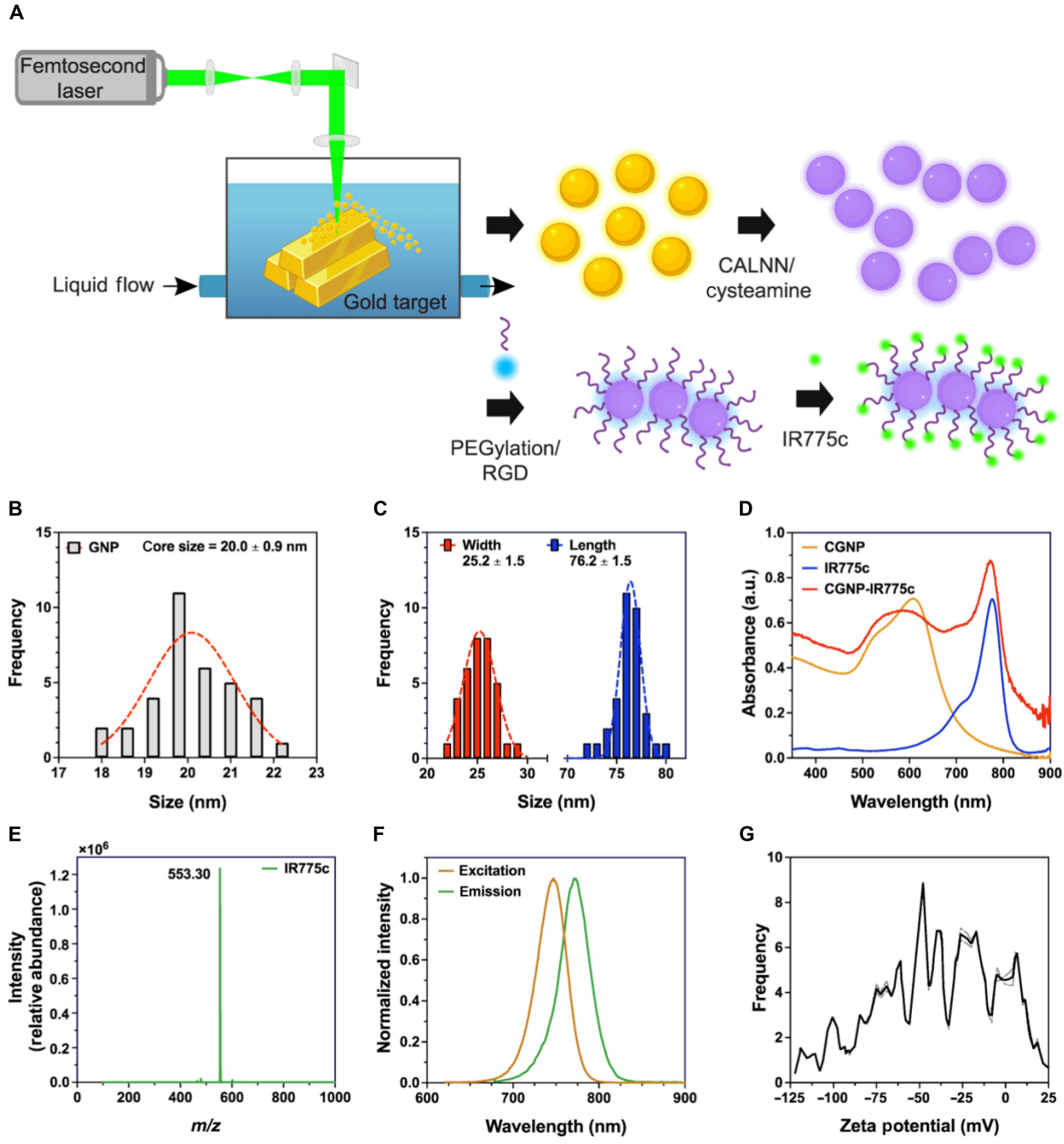

Fig. 2. Synthesis and comprehensive characterization of CGNP-IR775c. (**A**) Illustration of the synthesis of CGNP-IR775c. (**B**) Size distribution of GNP monomers by TEM analysis, showing monodisperse distribution with an average diameter of 20.0 ± 0.9 nm. (**C**) Morphological analysis of CGNP-IR775c showing a width of 25.2 ± 1.5 nm and a length of 76.2 ± 1.5 nm. (**D**) UV-Vis absorption spectra of CGNP (longitudinal SPR at 620 nm), IR775c dye (NIR absorption at 775 nm), and CGNP-IR775c conjugate in aqueous solution, demonstrating preserved dual-peak absorption spectrum. (**E**) Mass spectrometry of IR775c with a peak at *m/z* 553.30 confirms structural modification (ESI *m/z*): calculated for $C_{35}H_{41}N_2O_2S$ ($[M]^+$) 553.2883, found 553.2856. (**F**) Normalized fluorescence excitation (λ_{ex} = 750 nm) and emission (λ_{em} = 775 nm) spectra of IR775c. (**G**) Zeta potential distribution of CGNP-IR775c shown as mean of three independent measurements (bold black line). Gray dashed lines represent each individual measurement. Mean zeta potential: $\zeta = -39.63 \pm 0.95$ mV. Figure partially created in BioRender. Park, S. (2026) https://BioRender.com/5c8yiof.

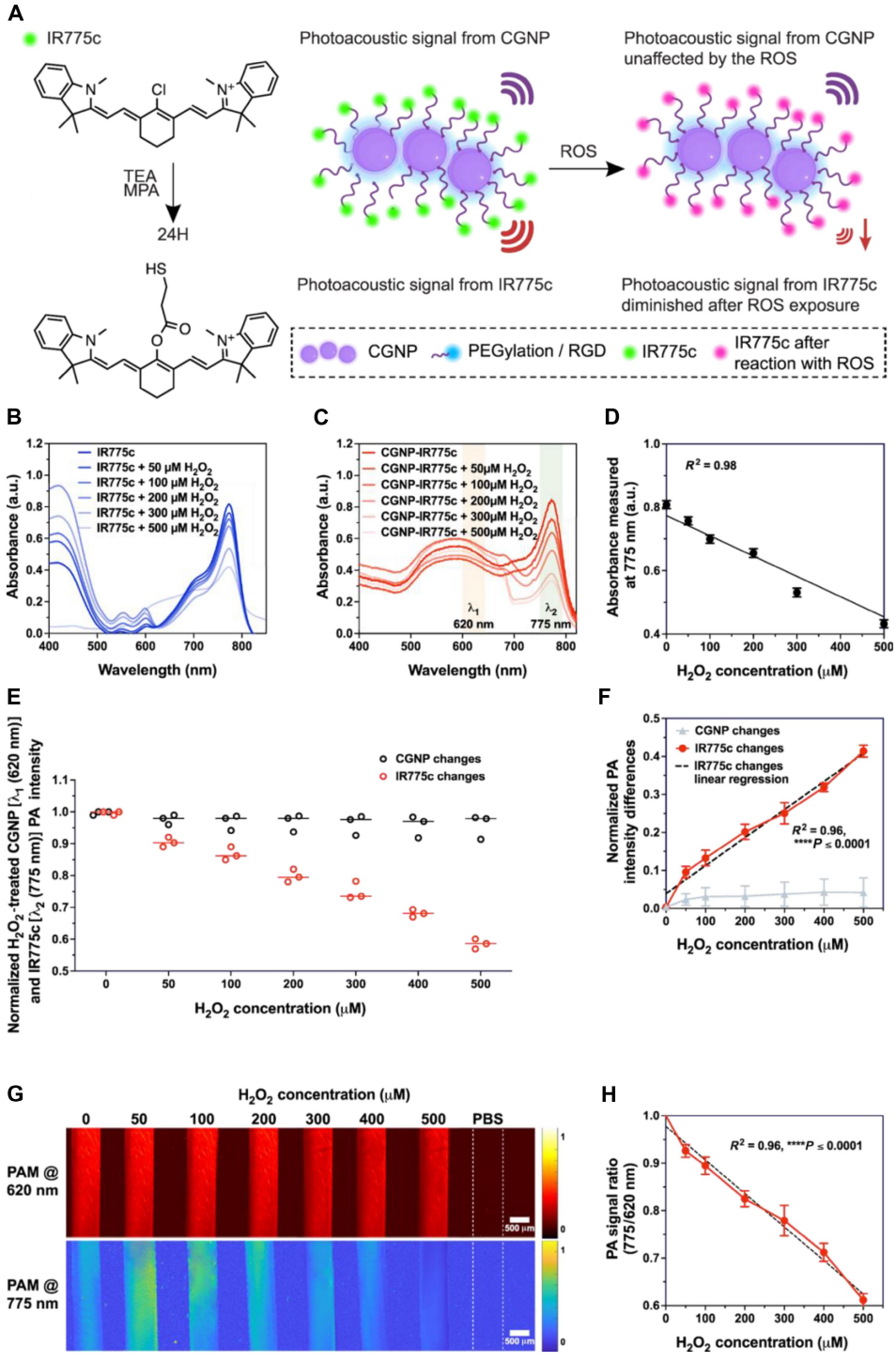

Fig. 3. ROS-responsive spectroscopic and PA properties of CGNP-IR775c. (**A**) Chemical synthesis and functional mechanism of ROS-responsive IR775c and schematic illustration of CGNP-IR775c structure and ROS-responsive behavior. Under physiological conditions, both CGNP and IR775c generate robust PA signals. Upon ROS exposure, selective oxidative quenching of the IR775c occurs, resulting in diminished PA signal at 775 nm while CGNP PA signals remain stable, enabling ratiometric detection. (**B**) UV-Vis spectra of free IR775c with increasing H_2O_2 (50 to 500 μM) showing concentration-dependent degradation. (**C**) UV-Vis spectra of CGNP-IR775c under identical conditions, showing selective attenuation at 775 nm while preserving 620-nm longitudinal SPR. (**D**) Quantitative analysis of normalized absorbance of CGNP-IR775c at 775 nm versus H_2O_2 concentration ($R^2 = 0.98$, $n = 4$). (**E**) PA amplitude measurements of CGNP-IR775c at 620 nm (CGNP) and 775 nm (IR775c) in silicone tube phantoms following H_2O_2 treatment. (**F**) Comparative normalized PA intensity showing differential ROS sensitivity between CGNP (620 nm) and IR775c (775 nm) with linear regression for IR775c ($R^2 = 0.96$, $^{****}P < 0.0001$). (**G**) Representative dual-wavelength (620 and 775 nm) PA images of silicone tube phantoms containing CGNP-IR775c before and after H_2O_2 treatment (50, 100, 200, 300, and 500 μM). Images acquired using a 27-MHz ultrasonic transducer. Scale bars, 500 μm. (**H**) Ratiometric analysis (I_{775}/I_{620}) versus H_2O_2 concentrations showing a linear relationship ($R^2 = 0.96$, $^{****}P < 0.0001$) for semiquantitative ROS detection.

resulted in concentration-dependent attenuation of the IR775c absorption peak at 775 nm. In particular, treatment with 500 μM H_2O_2 resulted in an ~50% decrease in absorbance (Fig. 3B). This response reflected oxidative disruption of the π-conjugation system (*47*, *48*). Notably, CGNP-IR775c exhibited enhanced sensitivity (~58% reduction at 500 μM H_2O_2) while maintaining stable plasmon absorption at 620 nm (Fig. 3C). This enhancement likely arose from gold nanoparticle (GNP)–mediated electron transfer processes that amplify ROS interactions at the IR775c interface (*49*, *50*). The linear correlation between H_2O_2 concentration and normalized absorbance at 775 nm ($R^2 = 0.98$) demonstrated quantitative dose-response behavior (Fig. 3D). Visual color change from green to pink at 500 μM H_2O_2 confirmed oxidative quenching of the IR775c chromophore (fig. S3).

PA validation using silicone tube phantoms confirmed these optical findings. The usefulness of CGNP clusters as an internal reference was validated by the fact that it maintained a constant PA amplitude throughout all H_2O_2 concentrations (ns, $P > 0.05$; Fig. 3E). Conversely, IR775c exhibited concentration-dependent PA signal reduction (***$P \leq 0.001$ for 50 μM and ****$P \leq 0.0001$ for 100, 200, 300, and 500 μM; Fig. 3E), with a strong linear relationship between normalized PA intensity and H_2O_2 concentration ($R^2 = 0.96$, ****$P \leq 0.0001$; Fig. 3F).

This differential response was detected using dual-wavelength PA imaging at 620 and 775 nm (Fig. 3G). Wavelength-specific ROS sensitivity was demonstrated by a gradual decrease in the PA signal at 775 nm with increasing H_2O_2 concentration, whereas the PA signal at 620 nm remained constant. Ratiometric analysis (I_{775}/I_{620}) yielded a linear correlation with H_2O_2 concentration ($R^2 = 0.96$, ****$P \leq 0.0001$), decreasing from 1.0 at baseline to 0.61 at 500 μM H_2O_2 (Fig. 3H). The physiologically relevant ROS levels during cellular stress and cellular death were reflected in the linear response throughout 50 to 500 μM H_2O_2, establishing CGNP-IR775c as a sensitive and semiquantitative platform for oxidative stress monitoring (*51*–*53*).

Cellular uptake, biocompatibility, and intracellular ROS detection

We confirmed biocompatibility and cellular internalization of CGNP-IR775c using ARPE-19 cells. After a 24-hour incubation period, confocal imaging revealed effective cytoplasmic accumulation of CGNP-IR775c (Fig. 4A). Distinct nuclear staining with 4′,6-diamidino-2-phenylindole (DAPI; blue), cytoplasmic labeling with CellTracker Green CMFDA (green), and CGNP-IR775c (red) were visible in the multiple channels. The signal overlap between CellTracker Green CMFDA and CGNP-IR775c was visible in the overlay image of yellowish-green areas. The colocalization with CellTracker Green CMFDA confirmed preferential cytoplasmic distribution, which is advantageous for monitoring intracellular ROS, as oxidative stress originates primarily from mitochondrial and cytoplasmic sources (*54*). Examination of the CGNP-IR775c fluorescence channel (Fig. 4A) revealed a subtle punctate, granular texture within the cytoplasmic distribution, rather than a uniformly diffuse signal, consistent with sequestration of CGNP-IR775c within numerous small vesicular structures dispersed throughout the cytoplasm following endocytic uptake (*55*–*58*). Bright-field imaging (Fig. 4B) provided corroborating morphological evidence of this particulate distribution, showing discrete electron-dense aggregates with a corresponding punctate pattern. This vesicle-consistent cytoplasmic distribution does not preclude ROS sensing from mitochondrial or cytoplasmic sources, as nanoparticles distributed throughout the cytoplasm have been shown to accumulate at perinuclear and mitochondrial microenvironments (*59*, *60*), and H_2O_2, a stable and membrane-permeable ROS species, readily diffuses across organelle membranes (*61*–*64*).

ARPE-19 cells maintained more than 80% viability at CGNP-IR775c concentration up to 400 μg/ml, demonstrating the high biocompatibility of CGNP-IR775c using the MTT assay (fig. S4). Up to 200 μg/ml (ns, $P > 0.05$), there was no discernible cytotoxicity, while cell viability dropped at 300 μg/ml (****$P < 0.0001$) and reached ~77% at 500 μg/ml. On the basis of this finding, we chose a CGNP-IR775c concentration of 50 μg/ml for subsequent studies to ensure minimal cytotoxicity and preserve optimal imaging performance.

After confirming the biocompatibility and cellular uptake of CGNP-IR775c in ARPE-19 cells, we further validated its biocompatibility directly in hiPSC-RPE cells, which are more representative of primary human RPE and are a clinically relevant cell type used in stem cell therapies. Cytocompatibility assays performed across a range of CGNP-IR775c concentrations (50 to 500 μg/ml) confirmed that hiPSC-RPE cells exhibited a viability profile consistent with ARPE-19 cells, with a consistently modest but acceptable reduction in viability compared to ARPE-19 cells across all concentrations. High viability (~95%) was maintained at the labeling concentration used throughout this study, confirming the biocompatibility of CGNP-IR775c in the clinically relevant cell type (Fig. 4C). These results provided direct validation to proceed with hiPSC-RPE cells for all subsequent functional assessments. Control hiPSC-RPE cells labeled with CGNP-IR775c showed strong red fluorescence throughout the cytoplasm in confocal microscopic images (Fig. 4D), indicating that IR775c chromophore was intact. Laser-treated cells exhibited a significant decrease in IR775c-induced fluorescence while maintaining DAPI nuclear staining after laser-induced oxidative stress (Fig. 4E), indicating that the signal decrease reflects ROS and oxidative stress–driven IR775c degradation during cellular death rather than imaging artifacts. Cell viability, quantified as the proportion of DAPI-positive nuclei retaining detectable IR775c fluorescence, decreased from ~94% in the control group to 76% in the laser-treated group (**$P \leq 0.01$; Fig. 4F), validating the effectiveness of the laser-induced cellular death model. Here, the "laser-treated" label refers to the laser-irradiated treatment condition rather than the uniform cellular state of all cells within the group, as ~76% of cells retained detectable IR775c signal and were classified as viable at the time of measurement. Normalized mean IR775c fluorescence intensity measured within IR775c-retaining viable cells showed ~90% signal reduction in the laser-treated group relative to the control group (**$P \leq 0.01$; Fig. 4G). These two metrics capture complementary aspects of the oxidative stress response in distinct cell populations. Figure 4F reflects the proportion of cells retaining sufficient IR775c signal to be classified as viable, while Fig. 4G demonstrates that this population had already undergone substantial oxidative quenching of IR775c, indicative of graded, sublethal ROS accumulation before overt cell death (*12*, *24*). This early-response sensitivity reflects the continuous nature of ROS-mediated IR775c degradation during the apoptotic process, and taken together, these results support CGNP-IR775c as a functionally responsive probe capable of reporting relative differences in cellular oxidative stress status, including sublethal ROS accumulation that precedes overt cell death.

All of these physicochemical and biological characteristics support the development of CGNP-IR775c as a biocompatible and functionally responsive contrast agent. The demonstrated optical characteristics allows for noninvasive, longitudinal monitoring of cell distribution

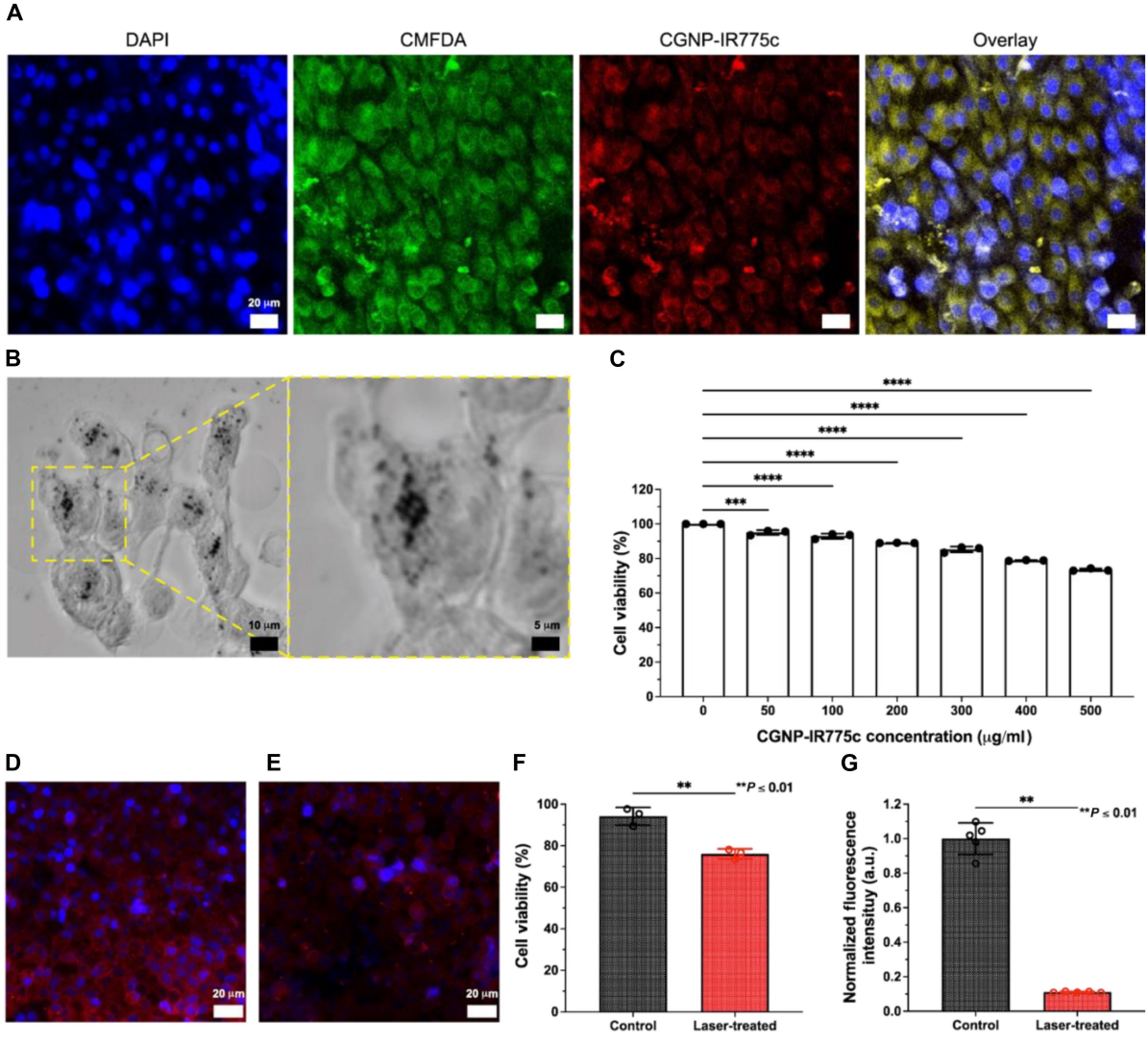

Fig. 4. Cellular uptake, biocompatibility, and ROS-responsive detection of CGNP-IR775c in RPE cells. (**A**) Confocal microscopy of CGNP-IR775c–labeled ARPE-19 cells. Nuclei stained with DAPI (blue, $\lambda_{ex} = 358$ nm, $\lambda_{em} = 461$ nm), cytoplasm labeled with CellTracker Green CMFDA (green, $\lambda_{ex} = 492$ nm, $\lambda_{em} = 517$ nm), CGNP-IR775c fluorescence (red, $\lambda_{ex} = 750$ nm, $\lambda_{em} = 775$ nm) showing a punctate, granular distribution throughout the cytoplasm, and overlaid image showing cytoplasmic colocalization. Scale bars, 20 μm. (**B**) Bright-field images providing corroborating morphological evidence of the punctate CGNP-IR775c distribution observed in the fluorescence channel (A), showing discrete electron-dense aggregates. Scale bar, 10 μm. The magnified inset highlights punctate CGNP-I R775c structures. Scale bar, 5 μm. (**C**) Concentration-response cytotoxicity analysis of CGNP-IR775c in hiPSC-RPE cells (0 to 500 μg/ml, 24-hour MTT assay). ***$P \leq 0.001$ and ****$P \leq 0.0001$. (**D** and **E**) Representative confocal images of hiPSC-RPE cells labeled with CGNP-IR775c (D) under normal conditions and (E) following laser-induced cellular death. Nuclei stained with DAPI are shown in blue, and CGNP-IR775c are shown in red. Scale bars, 20 μm. (**F**) Cell viability quantification showing the proportion of DAPI-positive nuclei retaining detectable IR775c fluorescence in the control (no laser irradiation) and laser-treated (laser-irradiated) groups. Note that laser-treated denotes the experimental treatment condition rather than the uniform cellular state of all cells within the group, as ~76% of cells in this group retained detectable IR775c signal and were classified as viable at the time of measurement (**$P \leq 0.01$). (**G**) Normalized mean IR775c fluorescence intensity measured within IR775c-retaining viable hiPSC-RPE cells, comparing control versus laser-treated groups, demonstrating substantial oxidative quenching of IR775c even among cells not yet classified as dead by the binary criterion in (F) ($n = 5$ independent experiments, **$P \leq 0.01$).

and viability, and its effective cellular uptake allows for accurate cell labeling without sacrificing cellular viability or function. These attributes demonstrate its potential for imaging stem cell behavior and viability, which is directly related to monitoring stem cell treatment outcomes.

PAM for semiquantitative cellular viability assessment in vitro

We used dual-wavelength PAM on hiPSC-RPE cells in both control and laser-treated groups to demonstrate viability monitoring capabilities. This approach provides an oxidative stress assessment by using the difference in ROS sensitivity from IR775c signals and the stability of CGNP signals.

Control hiPSC-RPE cells exhibited robust PA signals at both wavelengths, reflecting stable CGNP properties and intact IR775c chromophore with negligible oxidative stress (Fig. 5A). Following laser-induced cellular death, the PA signal at 620 nm remained stable, serving as an internal reference, while the PA signal at 775 nm showed significant attenuation, confirming ROS-responsive IR775c

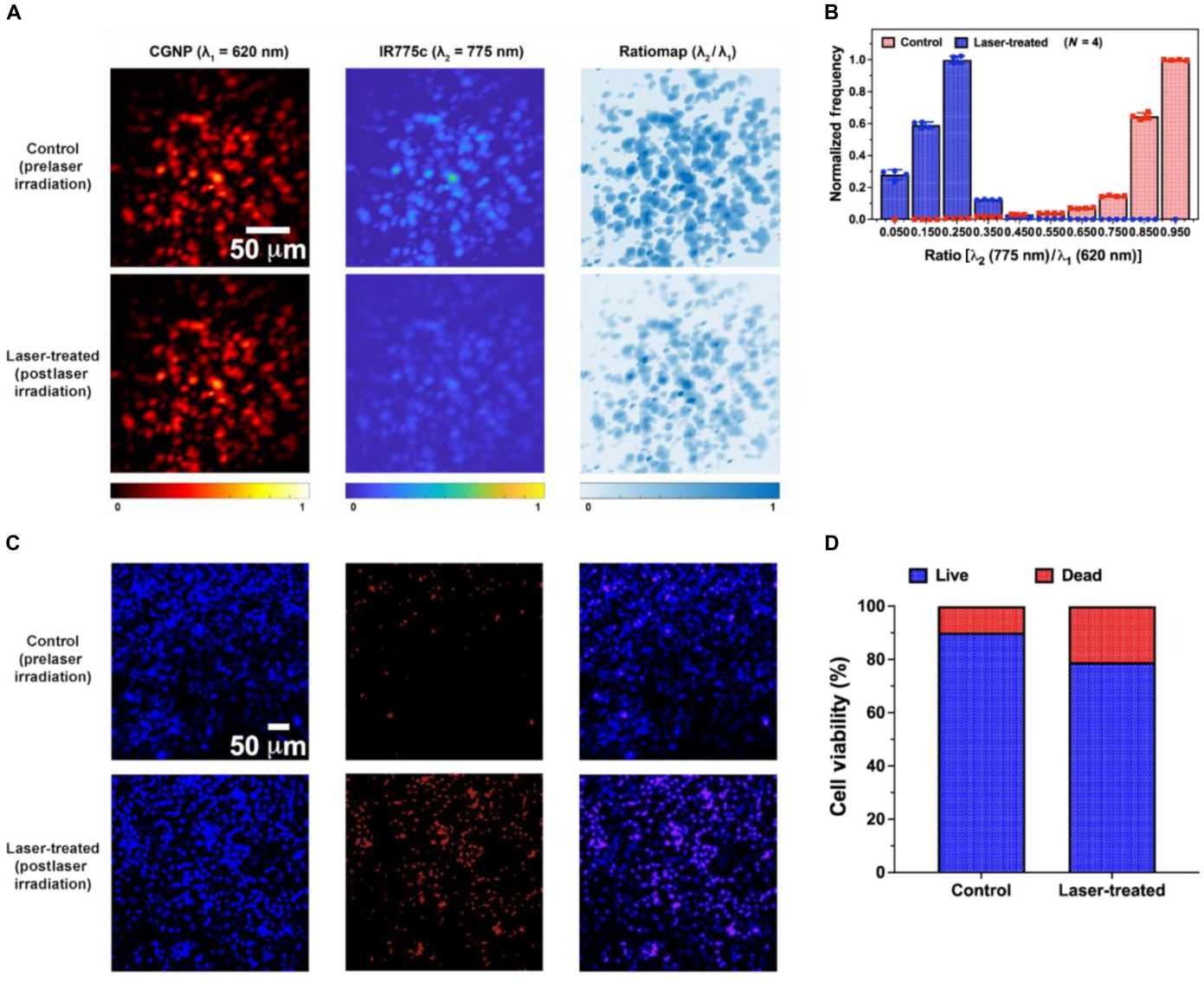

Fig. 5. Dual-wavelength PAM for semiquantitative cellular viability assessment of hiPSC-RPE cells in vitro. (**A**) Representative PAM images of CGNP-IR775c–labeled hiPSC-RPE cells acquired at $\lambda_1 = 620$ nm (CGNP signal, left) and $\lambda_2 = 775$ nm (IR775c signal, middle), and ratiometric maps (λ_2/λ_1) before (control) and after (laser-treated) laser-induced oxidative stress. Scale bar, 50 μm. Color bars represent normalized PA intensity (0 to 1). (**B**) Histogram analysis of PA signal ratios (I_{775}/I_{620}) from hiPSC-RPE cells, comparing control (blue) versus laser-treated (red) cells ($n = 4$ independent experiments). Histogram bins represent the relative frequency distribution of ratios ranging from 0.0 to 1.0. Distributions show minimal overlap, with control cells peaking at approximately 0.8 to 1.0 and laser-treated cells at approximately 0.1 to 0.3. (**C**) Representative fluorescence images of hiPSC-RPE cells stained with DAPI (blue, left) and propidium iodide (PI, red, middle), with merged overlay (right), in control (prelaser irradiation, top row) and laser-treated (postlaser irradiation, bottom row) groups. PI selectively labels cells with compromised membrane integrity, serving as an orthogonal ground truth measure of cell death independent of the IR775c signal. Scale bars, 50 μm. (**D**) Quantification of PI-based cell viability showing the proportion of PI-negative (live) and PI-positive (dead) cells in control and laser-treated groups. Cell viability decreased from ~90.10% in the control group to ~78.98% in the laser-treated group following laser irradiation (~21.02% nonviable cells), consistent with IR775c-based viability measured in Fig. 4F (~23.92% signal loss) and confirming the ground truth cell death fraction against which the PA ratiometric data in (B) are interpreted.

degradation. Pixel-by-pixel ratiometric analysis (I_{775}/I_{620}) provided normalized, semiquantitative viability maps with distinct spatial patterns. Control group cells displayed high ratios (approaching 1.0, blue), while laser-treated group cells showed low ratios (approaching 0.0, white), enabling identification of dead cells.

Histogram analysis revealed minimal overlap between control and laser-treated populations (Fig. 5B), demonstrating high sensitivity and specificity. Relatively low ratios in laser-treated cells (ratios 0.0 to 0.5) than those of the control group suggest low cellular viability due to oxidative stress, and a wide range of ratios may reflect different stages of cellular death or varying susceptibility to laser damage. In the control group, most of the ratios were above 0.7.

To establish an orthogonal ground truth measurement of cell viability independent of the CGNP-IR775c signal, live/dead fluorescence imaging was performed using DAPI and propidium iodide (PI) staining on hiPSC-RPE cells subjected to identical laser irradiation

conditions (Fig. 5C). PI staining, which selectively labels cells with compromised membrane integrity, confirmed that cell viability decreased from ~90.10% in the control group to ~78.98% in the laser-treated group, corresponding to ~21.02% nonviable cells within the laser-irradiated group (Fig. 5D). This value is in close agreement with the IR775c fluorescence–based viability estimate from Fig. 4, in which ~23.92% of cells exhibited complete IR775c signal loss under the same conditions. The strong concordance between these two independently obtained measurements provides mutual cross-validation and establishes a reliable ground truth benchmark for interpreting the PA ratiometric distributions in Fig. 5B. The predominant localization of laser-treated cells at PA ratios less than 0.25 in Fig. 5B is therefore consistent with the ~21 to 24% nonviable cell fraction confirmed by both independent methods, supporting the semiquantitative capability of the dual-wavelength PAM approach for relative viability assessment of CGNP-IR775c–labeled cells.

Longitudinal monitoring of transplanted cell viability in vivo

We performed longitudinal multimodal imaging in a rabbit model after subretinal injection of CGNP-IR775c–labeled hiPSC-RPE cells to evaluate clinical translation potential. We acquired images using color fundus photography, OCT, and multiwavelength PAM at the following consecutive time points: baseline on day 0 (pretransplantation), pre- and postlaser irradiation on day 4, and days 5, 6, 7, 9, 11, and 14 posttransplantation. This approach made it possible to evaluate the dynamics of cellular viability, tissue integrity, and graft integration longitudinally without causing any harm to the tissue.

En face color fundus photography showed the distribution and retention of hiPSC-RPE cells throughout the 14-day monitoring period (Fig. 6A). Transplanted cells appeared as localized pigmentation changes without evidence of blood vessel structural changes, hemorrhage, or retinal detachment, confirming the biocompatibility of both the cells and the safety of the treatment and imaging procedures. OCT cross-sectional images provided detailed structural information, clearly identifying retinal layers including the inner limiting membrane, ganglion cell layer, inner and outer plexiform layer, inner and outer nuclear layer, photoreceptor layer, choroid, and sclera (Fig. 6B). The hyperreflective signal in the subretinal space visible on day 4 indicated the presence of transplanted cells. From days 4 to 14, the cells gradually integrated into the host tissue, showing a stronger OCT signal intensity than the adjacent tissues. This enhanced OCT signal is likely attributable to both the increased optical scattering from a concentrated population of transplanted cells and the intrinsic contrast-enhancing properties of CGNPs, which have previously been shown to increase OCT signal intensity by up to 176% in vivo in a rabbit model (*65*). No complications such as hemorrhage, infection, or retinal detachment was observed throughout the entire period. These results suggest that the transplanted stem cells successfully integrated into the host tissues in the subretinal space.

Comprehensive observation of vascular anatomy, labeled cell distribution, and ROS-sensitive viability markers was achieved by multiwavelength PAM at 532, 620, and 775 nm, respectively. High-resolution vascular networks were captured by en face PAM at 532 nm, which also confirmed consistent imaging quality over the 14-day monitoring period and offered detailed retinal and choroidal networks that can be used as anatomical references (Figs. 6C and 7A).

At 620 nm, consistent PA signals from CGNP were observed at the transplantation site across all the time points (Figs. 6D and 7B), confirming persistent nanoparticle presence and stability as an internal reference standard. On the other hand, dynamic temporal alterations after laser-induced cellular death were shown by en face PAM at 775 nm (Figs. 6E and 7C). The PAM image on day 4 before laser irradiation revealed strong signals at 775 nm that were colocalized with signals at 620 nm, suggesting that the IR775c chromophores were intact in living cells. Following laser irradiation, there was a notable decrease in signal intensity at 775 nm but no change in signals at 620 nm. This confirmed ROS-responsive IR775c degradation under cellular death conditions and validated the stability of CGNP.

Ratiometric analysis (I_{775}/I_{620}) provided spatial distribution maps enabling semiquantitative assessment of heterogeneous cellular viability within the transplanted area. In areas without laser irradiation, high ratiometric values indicate healthy cells with intact IR775c, while the significant decrease in the ratio after laser irradiation suggests the sensitivity of the PA signal from IR775c to cellular death conditions. Overlay images combining 532-nm anatomical information with ratiometric viability data allowed us to determine the precise location and viability of transplanted hiPSC-RPE cells within complex retinal architecture (Figs. 6F and 7D).

To better visualize longitudinal changes in graft distribution and viability, enlarged PAM images were presented at key time points, including baseline on day 0 (pretransplantation), pre- and postlaser irradiation on day 4, and day 7 and 14 posttransplantation, as shown in Fig. 7. Although Fig. 6 illustrates the full time course of graft survival, the compact panel size constrains the ability to resolve fine spatial features. Figure 7 therefore complements Fig. 6 by providing magnified views at five representative time points, enabling direct visual comparison of CGNP and IR775c signal distribution before and after laser-induced cell death and facilitating a more precise spatial correlation between graft location and ratiometric viability signals. These expanded views enable clearer assessment of spatial cell distribution and signal changes reflecting cell viability within the same regions of interest over time.

Semiquantitative ratiometric analysis and spatiotemporal viability mapping

Cellular viability in non-laser-irradiated and laser-irradiated regions was illustrated over time through quantitative heatmap analysis (Fig. 8, A and B). Over the 14-day monitoring period, ratiometric values (I_{775}/I_{620}) in the non-laser-irradiated group (Fig. 8A) showed temporal stability, continuously clustering around 1.0. This consistent high viability at all time points suggests that there is little oxidative stress, preserved metabolic activity, and that transplanted hiPSC-RPE cells successfully engraft without experiencing any adverse effects on survival. The uniform distribution pattern indicates the functional integrity of CGNP-IR775c–labeled hiPSC-RPE cells in the subretinal environment. Different spatiotemporal patterns were seen in areas that were exposed to laser irradiation (Fig. 8B). The distribution matched well with ratios clustered around 1.0 before laser irradiation (day 4 pre), suggesting equal baseline viability. A noticeable change was observed immediately after laser treatment (day 4 post), with ratios falling to the 0.8 to 0.9 range, indicating acute ROS generation and IR775c degradation. A steady reduction persisted from day 5 through day 14, with ratio distributions ranging from 0.1 to 0.5. Instead of abrupt cell death, this temporal trend showed apoptotic process as a function of time, with cells undergoing varied degrees of oxidative damage. Spatial gradients of ROS exposure are suggested by the expanding distribution over time, which reflects cellular vulnerability to oxidative stress and distance from the laser irradiation

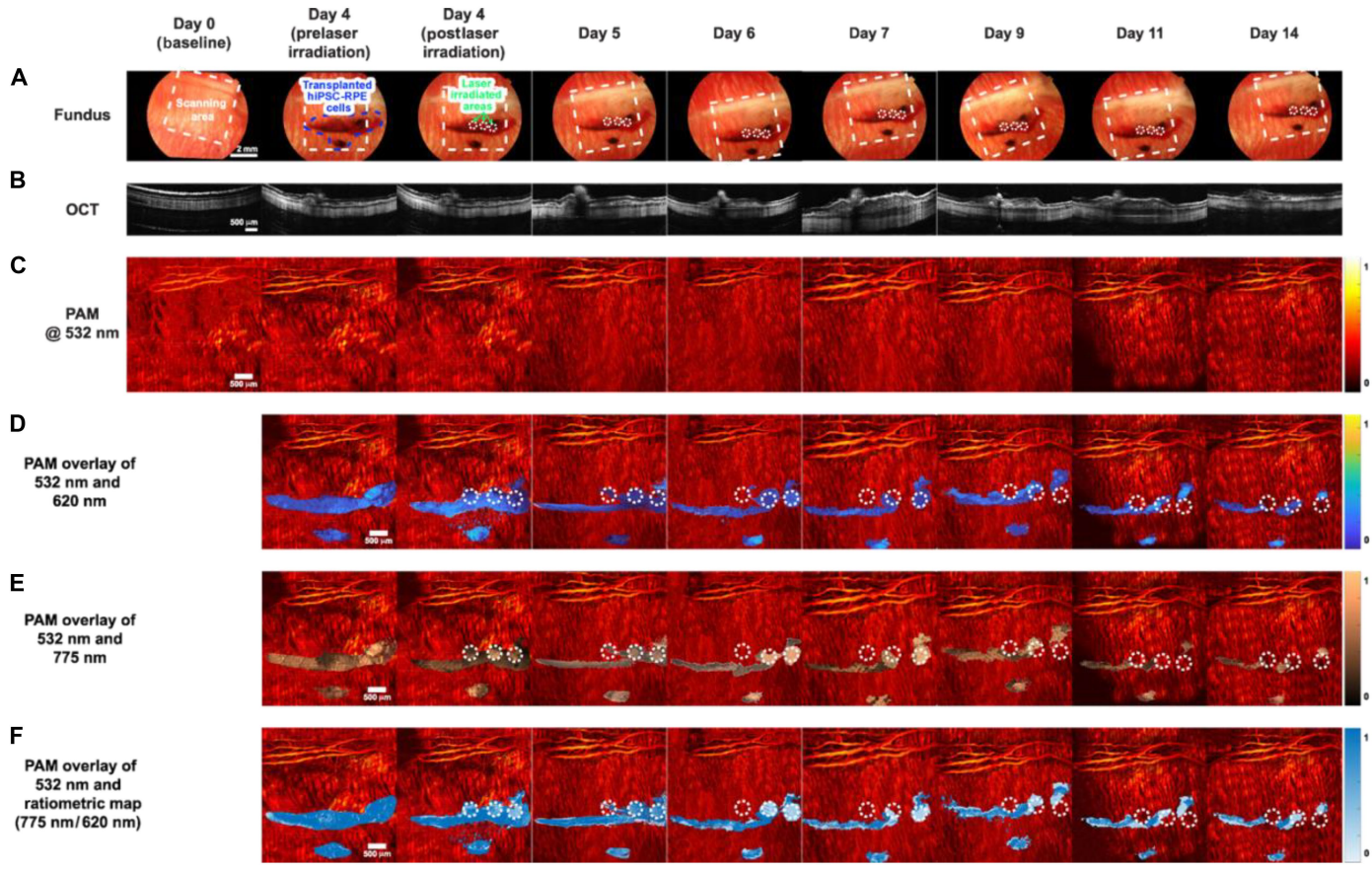

Fig. 6. Multimodal imaging assessment of hiPSC-RPE transplantation and laser-induced cellular death in vivo. Representative multimodal imaging (fundus photography, OCT, and PAM) data were acquired at baseline (day 0 pretransplantation) and day 4 pre- and postlaser irradiation, day 5, day 6, day 7, day 9, day 11, and day 14 posttransplantation to assess long-term cell survival and integration. (**A**) En face color fundus photography showing overall retinal morphology and vascular architecture with the cell transplantation site over time. (**B**) OCT cross-sectional images demonstrating retinal layer structure with a persistent transplanted cell layer. Scale bar, 500 μm. (**C**) En face PAM images at 532-nm wavelength showing endogenous hemoglobin contrast from retinal and choroidal vasculature with consistent signal across all time points. Scale bars, 500 μm. (**D**) En face coregistered overlay images combining PAM images at 532 nm showing tissue anatomy and PAM images at 620 nm displaying CGNP-specific PA signals from transplanted hiPSC-RPE cells, which remain stable throughout the monitoring period. Scale bar, 500 μm. (**E**) En face coregistered overlay images combining PAM images at 532 nm showing tissue anatomy and PAM images at 775 nm showing IR775c-specific signals that demonstrate responsiveness to cellular death conditions, with notable signal changes following laser-induced ROS generation (brown = relatively low ROS levels and healthy cells, black = relatively high ROS levels and dead cells). Scale bar, 500 μm. (**F**) En face coregistered overlay images combining PAM images at 532 nm showing tissue anatomy and functional information (ratiometric map, I_{775}/I_{620}) for comprehensive visualization of transplanted cell location and semiquantitative assessment of cellular death status within retinal architecture, with color-coded maps indicating relative viability levels through ROS levels. Higher ratios (blue) indicate greater cell viability. Scale bars, 500 μm.

focus (*66*, *67*). On day 14, most of the ratio values dropped below 0.2 to 0.3, indicating a significant loss of viable cells in the laser-irradiated area.

After the experimental endpoint, we conducted a histological examination to validate these PA imaging results. Well-preserved ocular architecture and obvious evidence of the transplanted stem cell engraftment within the host tissue were shown by hematoxylin and eosin (H&E) staining (Fig. 8C). Region-specific localization and morphological response after hiPSC-RPE transplantation were evident in the transplanted cells, which were distinguished by their characteristic brown nuclei. The retinal layers in non-laser-irradiated areas (the yellow dashed ovals in Fig. 8C) were structurally intact, suggesting a low level of inflammation. The laser-irradiated area (the red dashed oval in Fig. 8C), on the other hand, displayed cellular fragmentation and tissue damage, particularly in the outer limiting membrane. These findings indicate that laser irradiation results in both localized tissue structural disruption confined to the outer retina at the laser site and a pronounced local response by transplanted stem cells, with preservation of lamination in neighboring, nonirradiated tissue.

Although morphological changes in the laser-irradiated region were detected by H&E staining, direct detection of apoptosis-specific markers is necessary for a quantitative assessment of cellular viability at the molecular level. We accomplished this by using the terminal deoxynucleotidyl transferase–mediated deoxyuridine triphosphate nick end labeling (TUNEL) assay, a gold standard for determining the DNA fragmentation properties of apoptotic cells (*68*). In the same tissue section, representative fluorescence images showed distinct variations in cellular death status between laser-irradiated and nonirradiated regions (Fig. 8, D to F). Non-laser-irradiated areas showed minimal TUNEL-positive cells with only scattered positive cells likely representing normal background cellular death or tissue processing

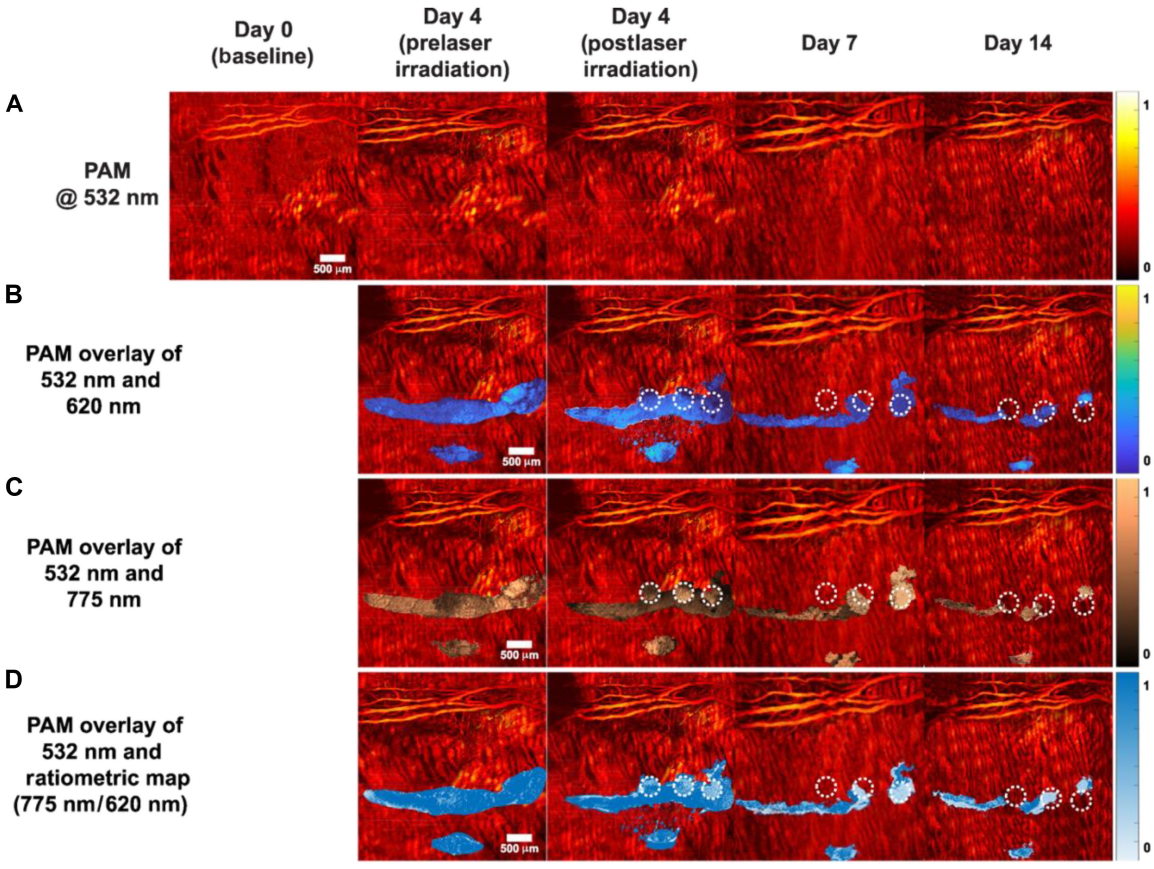

Fig. 7. Enlarged en face PAM visualization of longitudinal graft distribution and viability at key time points, including baseline (day 0 pretransplantation), day 4 pre- and postlaser irradiation, and day 7 and day 14 posttransplantation. (**A**) Representative PAM images at 532 nm showing tissue anatomy acquired at the key time points. Scale bars, 500 μm. (**B**) Coregistered overlay images combining PAM images at 532 nm and PAM images at 620 nm displaying CGNP-specific PA signals from transplanted hiPSC-RPE cells acquired at the key time points. (**C**) Coregistered overlay images combining PAM images at 532 nm and PAM images at 775 nm showing IR775c-specific signals that provide insights into cellular death conditions acquired at the key time points. (**D**) Coregistered overlay images combining PAM images at 532 nm and functional information (ratiometric map, I_{775}/I_{620}) for comprehensive visualization of transplanted cell location and semiquantitative assessment of cellular death status with retinal structure acquired at the key time points. Scale bar, 500 μm.

artifacts (Fig. 8, D and E, the yellow dashed ovals), although DAPI-stained nuclei (blue) were largely intact, indicating viable cells. On the other hand, the laser-irradiated area (Fig. 8, D and E, the red dashed oval) showed a large number of TUNEL-positive cells throughout the affected area, indicating widespread DNA fragmentation that is indicative of dead cells. The spatial distribution of TUNEL positivity closely matched the laser exposure area, demonstrating the localized and controlled property of the induced oxidative stress. The distinguishable signals between TUNEL-positive and TUNEL-negative regions confirmed that the laser-induced cellular death was confined to the targeted area without notable damage to surrounding tissues. Nuclear morphology assessment through DAPI staining (Fig. 8E) revealed that nuclei remained largely intact across both regions, with blue fluorescence visible throughout the tissue. The presence of DAPI-positive nuclei in the laser-irradiated area confirmed the continued presence of cells, while the IR775c-associated PAM signal was markedly reduced. This supports a ROS-responsive IR775c degradation rather than a disappearance of cells from the region of interest. The overlaid images combining TUNEL (green) and DAPI (blue) channels (Fig. 8F) provided a comprehensive visualization of cellular status. In nonirradiated regions, cells displayed DAPI-only staining, indicating viable cells with intact DNA. In laser-irradiated areas, the colocalization of TUNEL and DAPI signals (cyan) confirmed that TUNEL-positive cells contained fragmented DNA within morphologically identifiable nuclei. Quantitative analysis of cell viability by TUNEL assay revealed significant differences (Fig. 8G). Non-laser-irradiated areas showed minimal TUNEL positivity ($11.86 \pm 1.25\%$), confirming baseline cell viability. Laser-irradiated areas showed a significantly increased number of TUNEL-positive cells ($83.38 \pm 1.97\%$, $^{**}P \leq 0.01$, $n = 5$). The analysis from the TUNEL assay corroborates the PA ratiometric findings, with non-laser-irradiated areas maintaining high ratios and laser-irradiated regions exhibiting a marked decrease in ratios. Furthermore, the body weight of the animal was monitored at different time points (Fig. 8H). The results show that all animal weights gradually increased, indicating the overall safety of using CGNP-IR775c guided multimodal imaging for cell viability monitoring.

According to these findings, we could confirm that the observed differences between the two groups in morphology, TUNEL positivity, and PA ratios were due to laser-induced cellular alterations. This strengthens the validation of our PA imaging approach and confirms that CGNP-IR775c can detect cellular-level death status changes

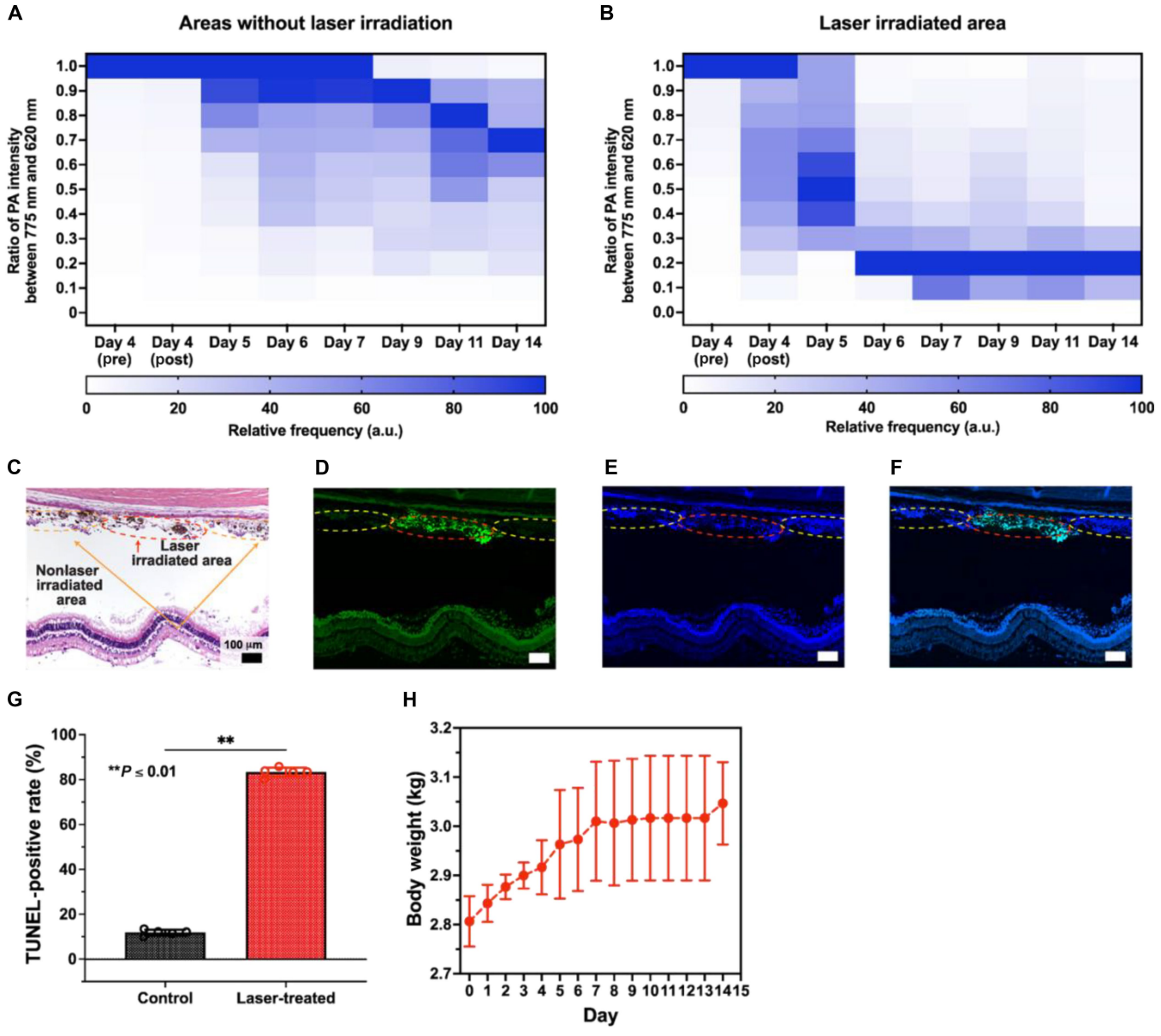

Fig. 8. Quantitative spatiotemporal analysis of transplanted cell viability through ratiometric heatmap and histological validation of laser-induced cellular death. Heatmap analysis of the 775/620 ratio distribution in (**A**) non-laser-irradiated and (**B**) laser-irradiated regions over 14 days. Nonirradiated regions maintained high viability throughout, whereas irradiated regions declined from a ratio of ~1.0 before irradiation (day 4) to ~0.8 immediately after irradiation, with continued decline through day 14. For each day, color indicates region of interest pixel frequency across ratio bins, peak-normalized so that the maximum bin equals 100 a.u., to visualize changes in distribution shape over time. (**C**) H&E staining of the retinal tissue showing laser-irradiated versus nonirradiated areas. The yellow dashed ovals indicate non-laser-irradiated areas, while the red dashed oval points to the laser-irradiated area. (**D**) Fluorescence microscopy image showing TUNEL-positive cells (green), indicating DNA fragmentation and apoptosis. The red dashed oval shows the laser-irradiated region containing numerous TUNEL-positive cells, while the yellow dashed ovals show the non-laser-irradiated region with minimal positive staining. (**E**) DAPI nuclear staining (blue) of the same tissue section demonstrates intact nuclear morphology in viable cells. (**F**) Overlaid image combining TUNEL (green) and DAPI (blue) channels. Scale bars, 100 μm. TUNEL-positive apoptotic cells (cyan, colocalization of green and blue) are localized in the laser-irradiated area, while nonirradiated areas maintain DAPI-only staining, indicating viable cells. (**G**) Quantitative analysis of TUNEL-positive cell percentage comparing nonirradiated (control) versus laser-irradiated regions. (**H**) Body weight of rabbits over the 14-day monitoring period. All rabbits showed a steady increase in body weight, reflecting normal growth and general health.

that correlate with both structural disruption and DNA fragmentation. The strong agreement between longitudinal PA measurements, morphological assessment, and molecular detection establishes dual-wavelength PAM with ROS-responsive CGNP-IR775c as a robust, noninvasive platform for longitudinal monitoring of stem cell viability in vivo with sensitivity comparable to molecular histological assays.

DISCUSSION

Using CGNP-IR775c as a contrast agent, our ratiometric PAM allows for longitudinal, noninvasive monitoring of the viability of transplanted stem cells in vivo. As validated in both in vitro cellular models and a clinically relevant rabbit model in vivo, this method offers sensitivity in relatively assessing cell viability comparable to gold-standard histology

assays. The strong correlation between PA ratiometric measurements, morphological assessment (H&E), and molecular apoptotic detection (TUNEL) demonstrates the promising potential of this approach as a tool for tracking cell therapies in living tissues. These results address a fundamental limitation of regenerative medicine, which is the inability to monitor the fate of transplanted cells without tissue damage and over extensive time.

The ROS-responsive mechanism of CGNP-IR775c provides molecular sensitivity to cellular stress and cellular death. During cellular death, elevated intracellular ROS levels induce oxidative quenching of the IR775c heptamethine backbone, resulting in a reduced PA signal at 775 nm. In contrast, the CGNP maintains a stable PA signal at 620 nm, serving as an internal reference. This ratiometric approach addresses the limitations of single-wavelength imaging with signal amplitude influenced by variables such as local excitation laser fluence and contrast agent concentration. In our experimental model, we observed a progressive decrease in the PA signal ratio between 775 and 620 nm over the 14-day time period following laser-induced cellular death, revealing distinct temporal phases of cellular response. Notably, a more gradual decline in the PA signal ratio was also observed in the non-laser-irradiated region beginning from day 9, which is discussed further in the context of the immunological limitations of this xenograft model. The initial rapid decrease in the PA signal ratio corresponds to direct degradation of IR775c by ROS generated during the acute phase of laser-induced cell death, whereas the subsequent gradual reduction in the PA signal ratio may reflect, at least in part, secondary inflammatory responses and cellular clearance mechanisms (*7*, *69*), although further investigation is required to confirm this hypothesis. This temporal resolution enables continuous monitoring of the cellular stress trajectory, distinguishing our approach from endpoint histological methods that only capture snapshots at discrete time points. Because this monitoring is noninvasive, the ability to track these dynamic changes may help identify critical time points at which clinical assessment or intervention would be most informative.

Current monitoring of RPE transplantation relies on OCT for anatomical assessment and functional tests such as visual acuity measurements and electroretinography, performed weeks to months following transplantation. Although these methods provide valuable information regarding the status of the overall retina, they provide limited insight into the cellular details, particularly in the critical early posttransplantation phase during which cellular fate is decided. Multiwavelength PA imaging powered by CGNP-IR775c addresses this pivotal gap by facilitating early detection of elevated oxidative stress and declining cell viability. This could potentially enable the identification of patients who may benefit from timely reevaluation of therapeutic strategies, such as adjustment of immunosuppression or supportive antioxidant treatment (*70*), although the clinical efficacy of such interventions in this context remains to be established. Moreover, the ratiometric measurement provided by this approach offers a relative, semiquantitative indicator of cell viability that may complement existing clinical assessment tools, thereby supporting data-driven therapeutic management that goes beyond subjective evaluation. Furthermore, the ROS-responsive mechanism has applicability beyond ophthalmology, as oxidative stress represents a common pathway leading to transplant failure across several regenerative medicine applications. This technology holds potential for adaptation to monitor stem cell therapies in other organs where viability assessment would enhance clinical outcomes, such as heart, liver, or brain (*71*–*73*).

While our findings demonstrate the potential of PAM combined with CGNP-IR775c for viability monitoring, several limitations should be considered. These relate to (i) the scale and design of the current in vivo validation, (ii) the specificity of the PA signal in distinguishing true graft viability from confounding biological processes, and (iii) the broader scope of future validation required for clinical translation.

1) Scale and design of the current in vivo validation. The in vivo validation in this study was performed in a limited number of rabbits, which represents a modest sample size for drawing statistically robust conclusions. This study was intended as an initial proof-of-concept evaluation of the CGNP-IR775c imaging platform in a clinically relevant animal model, with the primary aim of demonstrating technical feasibility rather than establishing statistical efficacy. Future studies with larger animal cohorts will be necessary to assess inter-animal variability, improve statistical power, and further validate the semiquantitative capabilities of this approach before clinical translation. Relatedly, although meloxicam and corticosteroid treatment were administered to minimize inflammation and immune-mediated rejection in this xenograft model, a gradual decline in PA viability signal was observed beginning from day 9 even in areas that did not receive laser irradiation. This observation suggests that the immunosuppressive treatment may have provided incomplete protection against T cell–mediated xenograft rejection inherent to the transplantation of hiPSC-RPE cells into immunocompetent rabbits (*74*–*77*). While this represents a limitation of the current animal model for isolating intrinsic graft biology from immune-mediated effects, the CGNP-IR775c platform may offer earlier detection of graft deterioration than what is typically achievable with conventional anatomical imaging alone. Future studies using more comprehensive immunosuppressive protocols or autologous or syngeneic transplantation models will help to better distinguish immune rejection from intrinsic graft failure dynamics.

2) Specificity of the PA signal. The laser photocoagulation model used to induce cell injury in this study primarily acts via a thermal mechanism, with melanin within RPE cells absorbing 532-nm light and converting it to heat (*78*, *79*). Thermal injury of this nature has been shown to elicit a temporally mixed cell death response. In an in vitro model of photocoagulation, a transient peak in necrosis was observed at ~6 hours postirradiation, followed by a subsequent rise in apoptotic features at ~24 hours (*80*). This biphasic pattern suggests that neither necrosis nor apoptosis alone fully characterizes the cellular response to photocoagulation. CGNP-IR775c detects changes in intracellular ROS via oxidative quenching of the IR775c moiety, and elevated ROS is a common downstream feature of both necrotic and apoptotic processes (*21*, *81*). However, ROS-mediated cell death in RPE cells does not necessarily proceed through canonical caspase-dependent apoptotic pathways. Oxidative stress–induced RPE cell death has been reported to exhibit necrotic rather than apoptotic features and might be insensitive to caspase inhibition (*82*). Therefore, while pathway-specific assays, including markers of necrosis and caspase activity assays where apoptotic contribution is suspected, could provide complementary information about the nature of cell death underlying the observed PA signal changes, such characterization was beyond the scope of the present study. The PA signal reported here should be interpreted as a general indicator of ROS-associated loss of cell viability, without implying specificity for any particular cell death pathway. Beyond ROS-mediated oxidative quenching, other mechanisms may also contribute to attenuation of the IR775c PA signal. These include photobleaching of the IR775c chromophore

under repeated laser excitation (*83*) and other potential physicochemical alterations under intracellular conditions, the contributions of which remain to be systematically characterized in future studies. However, the ratiometric design of CGNP-IR775c intrinsically compensates for signal changes that affect both the 775- and 620-nm channels equally since such perturbations would not alter the signal ratio. Signal reduction mechanisms that selectively affect only the IR775c channel remain an important consideration and will be systematically investigated in future studies. A related consideration concerns the in vivo fate of CGNP-IR775c following transplanted cell death. As demonstrated in our previous study (*19*, *84*), CGNP present in dead cells or freely injected into the subretinal space is phagocytosed by macrophages and cleared from the retinal tissue. Therefore, following cell death in the present study, the released CGNP-IR775c is expected to be taken up by macrophages and progressively removed from the subretinal space over time. This clearance process is consistent with the continued decline in both PA signal components observed in the laser-irradiated group throughout the longitudinal monitoring period and does not confound the ratiometric viability readout within the experimental window of this study.

3) Scope of future validation. Although the laser-induced cellular death model with controlled oxidative stress effectively validates our imaging approach, other pathological conditions, such as ischemic injury or immunological rejection, may exhibit distinct ROS kinetics that could differentially affect signal dynamics. Comprehensive validation across diverse graft failure models would enhance the clinical applicability of this technology. In addition, correlations observed between TUNEL assay results and PA measurement were established at the level of cell clusters. Single-cell imaging and analysis would provide more comprehensive morphological, functional, and cellular information, enabling deeper mechanistic insights. Last, despite confirmation of biocompatibility in our study, clinical translation necessitates extensive toxicological evaluations conducted according to the regulatory standards for medical devices and contrast agents.

In summary, we have demonstrated that PAM using CGNP-IR775c enables relative, semiquantitative, noninvasive, and longitudinal assessment of transplanted stem cell viability with sensitivity at the cellular level. This work addresses a critical unmet need in regenerative medicine by providing a platform that combines high spatial resolution, longitudinal monitoring capability, and cellular specificity for viability assessment. This initial validation across in vitro models, in vivo longitudinal imaging, and histological assessment provides a promising basis for further development toward clinical translation. Beyond ophthalmology, the ratiometric PAM strategy presented here offers a versatile platform applicable to a broad range of therapeutic applications. Given the global expansion of stem cell therapies in numerous applications, technologies that allow for longitudinal monitoring of cellular viability and function without causing tissue damage will be essential for optimizing treatment protocols and improving treatment outcomes. This study demonstrates that ROS-responsive contrast agents powered PAM represent a promising approach with potential for relative viability quantification, enabling improved tracking and management of stem cell therapies in regenerative medicine.

MATERIALS AND METHODS

Multimodal imaging system design

A multimodal imaging system was developed that integrates triple-wavelength PAM and OCT for noninvasive, longitudinal tracking and viability monitoring of transplanted stem cells (Fig. 9). The primary excitation source for PAM was a pulsed green fiber laser (GLPM-10, IPG Photonics, Marlborough, MA, USA) with a center wavelength of 532 nm, a pulse duration of 1.3 ns, a maximum output power of 10 W, and an adjustable pulse repetition rate of 10 to 300 kHz. Wavelength tuning was achieved through stimulated Raman scattering using a single-mode fiber (100 m SMF-28, Corning, NY, USA), enabling spectral shifts to 620 to 775 nm to match the absorption peaks of CGNP clusters and IR775c dye, respectively. The acquired spectrum containing the Raman Stokes peaks was measured using a spectrometer and is shown in fig. S1. Stokes waves were generated via nonlinear interactions between pump photons and vibrational modes in the fiber medium, producing emission at longer wavelengths (*85*–*87*). These emissions were confirmed using a fiber optic spectrometer, with bandpass filters applied to isolate specific wavelengths.

PA signals were detected using a custom-built 27-MHz needle-type ultrasound transducer with 60% bandwidth (Optosonic Inc., Arcadia, CA, USA). The signals were amplified using a low-noise preamplifier and digitized by a 250-MHz high-speed digitizer (RazorMax PCIe CSE161G4, Gage, Lockport, IL, USA). A spectral domain OCT system using a 1300-nm light source (TEL321, Thorlabs, Newton, NJ, USA) was coaxially integrated into the PAM setup. The combined optical paths were collimated and focused through an ophthalmic lens and scan lens (LSM03-BB, Thorlabs Inc., Newton, NJ, USA), with two-dimensional scanning enabled via a galvanometer mirror. An acquisition time for a scanning area of 512 by 512 points was 1.75 s. Laser pulse energies at the focal plane were maintained at 80 nJ per pulse, which is well within the American National Standards Institute (ANSI) safety thresholds for ocular exposure. All optical parameters in this study adhered to ANSI Z136.1 standards. MATLAB (MathWorks, Natick, MA, USA) was used to program the trigger control and data acquisition in coordination with the DAQ card and OCTP-1300 scanning head library.

Synthesis and functionalization of CGNP-IR775c

CGNP clusters were fabricated through the self-assembly of capping agent-free spherical GNP monomers produced by using the unique physical method of femtosecond pulsed laser ablation (PLA) (*65*, *84*). In the typical process, GNP monomers were first generated via PLA of a bulk gold target (99.999% purity; EJTAuXX502A2, Kurt J. Lesker Company, Jefferson Hills, PA, USA) immersed in flowing deionized water (18 MΩ·cm) containing 30 μM NaCl using a ytterbium-doped femtosecond fiber laser (FCPA μJewel D-10k, IMRA America, Ann Arbor, MI) operating at 1.045 μm, with a repetition rate of 100 kHz, a pulse duration of 700 fs, and a pulse energy of 50 μJ. The resulting colloidal solution contained GNP monomers with an average diameter of 20 nm and a narrow size distribution, exhibiting a localized surface plasmon resonance at 520 nm. Following the fabrication of GNP monomers, they were assembled into CGNP clusters by sequentially modifying their surface with two different ligands, including a custom-synthesized pentapeptide, Cys-Ala-Leu-Asn-Asn (CALNN, >95% purity, used without further purification, RS Synthesis, Louisville, KY, USA) and cysteamine hydrochloride (M6500-25G, Sigma-Aldrich, St. Louis, MO, USA), via exploiting the strong anchoring of the Au-sulfur bonds. Only minimal amounts of CALNN peptide and cysteamine hydrochloride, sufficient for inducing structurally stable CGNP clusters, were used to ensure that enough space was left on the surface of CGNP clusters for subsequent PEGylation, RGD peptide conjugation, and IR775c functionalization. Specifically, the colloidal

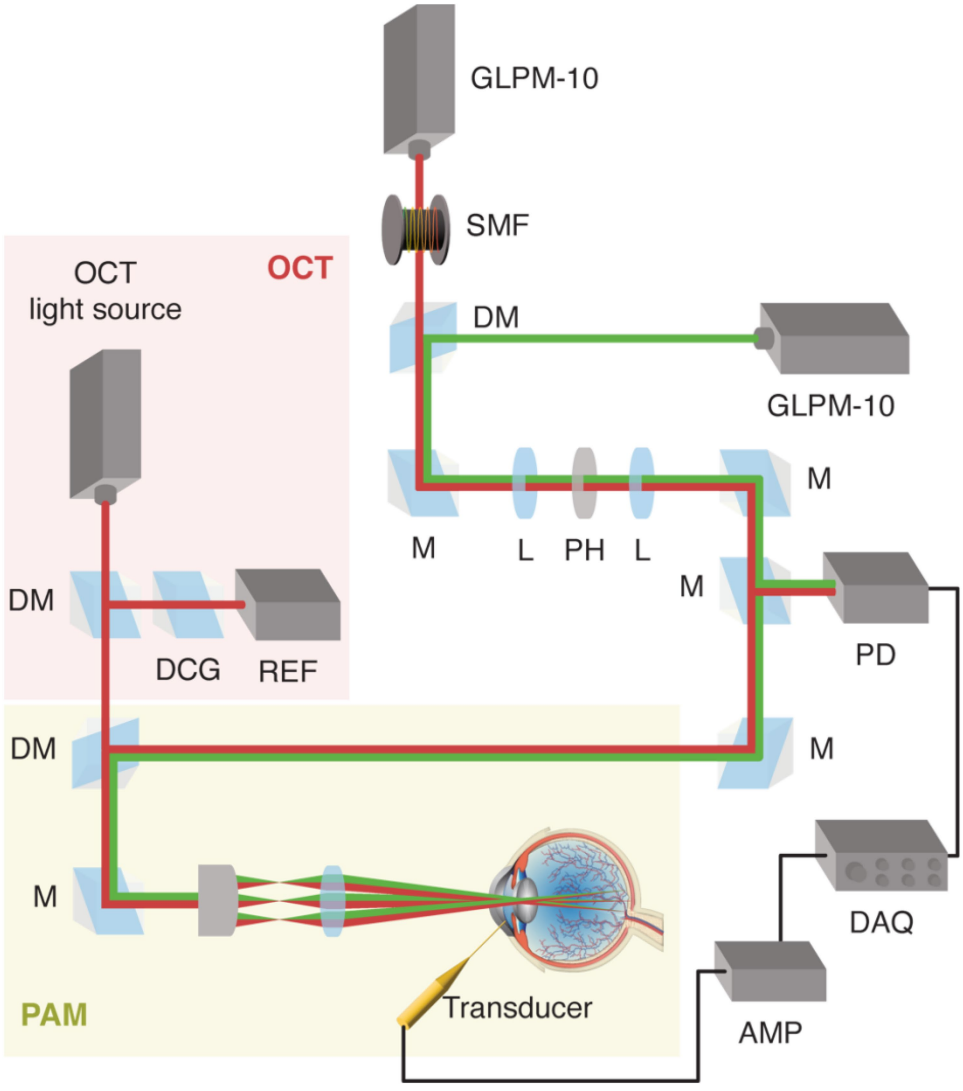

Fig. 9. The schematic of the triple-wavelength PAM and OCT multimodality imaging system. SMF, single-mode fiber; DM, dichroic mirror; M, mirror; L, lens; PH, pinhole; PD, photodiode; DCG, dispersion compensation glass; DAQ, digital acquisition; REF, reference.

solution of GNP monomers was first mixed with CALNN at a molar ratio of 2000:1 (CALNN:GNP) and incubated for 2 hours at room temperature. Then, cysteamine hydrochloride was subsequently added at a molar ratio of 1800:1 (cysteamine:GNP). This mixture was left undisturbed until a color change from red-pink to blue was observed (typically within 24 hours to several days), indicating self-assembly of GNP monomers into CGNP clusters. Successful formation of red-absorbing CGNP clusters was further confirmed by UV-Vis spectroscopy, which exhibited two distinct surface plasmon resonance (SPR) bands: a weak transverse SPR at approximately 520 nm and an intense , redshifted longitudinal SPR around 620 nm. The obtained CGNP clusters were then isolated by centrifugation and resuspended in deionized water at a mass concentration of 0.5 mg/ml.

Furthermore, to enhance biocompatibility and cellular uptake, the as-prepared CGNP clusters were conjugated with both PEG molecules and RGD peptides (*65*, *88*). Briefly, 20 μl of 1 mM thiol-terminated PEG with a molar mass of 2000 g mol^{-1} (mPEG-SH, MW 2k, PLS-605, Creative PEGWorks, Durham, NC, USA) was added to 5 ml of CGNP clusters (optical density = 10 at 620 nm), corresponding to a molar ratio of 400:1 (mPEG-SH:GNP monomers within the CGNP clusters), and the mixture was incubated for 2 hours at room temperature to allow PEGylation. Subsequently, the PEGylated CGNP clusters were reacted with 60 μl of 1 mM custom-synthesized RGD peptide (RGDRGDRGDRGDPGC, >95% purity, used without further purification, RS Synthesis, Louisville, KY, USA), corresponding to a molar ratio of 1200:1 (RGD:GNP monomers in CGNP clusters), for another 2 hours at room temperature. After this reaction, the resulting PEGylated CGNP clusters conjugated with RGD peptides were collected by centrifugation at 1000*g* for 30 min and resuspended in 4 mM borate buffer (pH 8.2), containing bovine serum albumin (5 mg/ml; A9418-50G, Sigma-Aldrich, St. Louis, MO, USA). The borate buffer was prepared from using boric acid (B0394-100G, Sigma-Aldrich, St. Louis, MO, USA) with pH adjustment using sodium hydroxide (221465-500G, Sigma-Aldrich, St. Louis, MO, USA). The

final suspension of PEGylated CGNP clusters conjugated with RGD peptides was adjusted to a mass concentration of 0.5 mg/ml.

Last, the CGNP clusters were functionalized with IR775c so that the generated conjugates (CGNP-IR775c) could serve as PAM image contrast agents for not only tracking the location but also assessing the viability of the transplanted hiPSC-RPE cells. This is because IR775c is highly sensitive to elevated levels of ROS, a key mediator of cellular death. IR775c was synthesized from IR775 through the substitution of the chlorine side group with a carboxylic acid moiety (*20*). Briefly, 50 mg of IR775 (544914, Sigma-Aldrich, St. Louis, MO, USA) was dissolved in 0.5 ml of *N*,*N*′-dimethylformamide (DX1727, Sigma-Aldrich, St. Louis, MO, USA) and reacted with 10 μl of 3-mercaptopropionic acid (8.05967, Sigma-Aldrich, St. Louis, MO, USA) and 21 μl of triethylamine (8.08352, Sigma-Aldrich, St. Louis, MO, USA) for 24 hours at room temperature. The reaction was quenched with excess dichloromethane (DCM; D37, Thermo Fisher Scientific, Wilmington, MA, USA), and the organic phases were washed with brine before being dried over anhydrous Na_2SO_4 (S421-500, Thermo Fisher Scientific, Wilmington, MA, USA). IR775c was then purified via flash chromatography over P60 irregular silica (R12030B, Silicycle, Québec, Québec, Canada) using 3% methanol (A412, Thermo Fisher Scientific, Wilmington, MA, USA) in DCM as the mobile phase. After obtaining IR775c, functionalization of CGNP clusters was performed by mixing them with IR775c at a 1:1 molar ratio, optimized through UV-Vis and fluorescence spectroscopy to maximize dye loading while minimizing any quenching effects.

Characterization of CGNP-IR775c

CGNP-IR775c was characterized using multiple complementary techniques. The absorption spectra were measured using UV-Vis spectroscopy (UV-3600, Shimadzu Corp., Kyoto, Japan), and the fluorescence emission spectra of IR775c were obtained using a fluorometer (FluoroMax-3, Horiba, Kyoto, Japan). The morphology and size distribution of CGNP-IR775c were analyzed via TEM (Talos F200X G2, Thermo Fisher Scientific, MA, USA) at an accelerating voltage of 200 kV. Sample solutions were deposited onto 400 mesh carbon-coated copper grids and dried at room temperature before imaging. Hydrodynamic diameter and size distribution were evaluated using dynamic light scattering (DynaPro NanoStar, WYATT Technology, CA, USA). Surface charge of CGNP-IR775c was measured using zeta potential analysis (Zetaview Quatt, ParticleMetrix, Ammersee, Germany). The molecular weight and purity of IR775c were confirmed by mass spectrometry (Nexion 2000, PerkinElmer, MA, USA) and a ^{1}H nuclear magnetic resonance spectrometer [Varian MR400 Cobalt, Varian Inc. (now Agilent Technologies), CA, USA]. All measurements were performed at room temperature under standardized conditions to ensure reproducibility.

Cell culture

The ARPE-19 cell line, derived from human RPE, was cultured in Dulbecco's modified Eagle's medium/nutrient mixture F-12 (11320033, Gibco, Waltham, MA, USA) supplemented with 15 mM Hepes (H4034, Sigma-Aldrich, St. Louis, MO, USA), L-glutamine (G8540, Sigma-Aldrich, St. Louis, MO, USA), 10% fetal bovine serum (FBS; 35-010-CV, Corning, NY, USA), sodium bicarbonate (1.16 g/liter; S5761, Sigma-Aldrich, St. Louis, MO, USA), and 5% (v/v) antibiotic-antimycotic solution (15240062, Gibco, Waltham, MA, USA). Cells were maintained at 37°C in a humidified 5% CO_2 incubator with media replacement every 2 to 3 days.

hiPSCs were generated from fibroblast-derived iPSCs (Lagen Laboratories, line 006-BIOTR-0001, clone 1) following protocols approved by the University of Michigan Human Pluripotent Stem Cell Research Oversight Committee (#1099). Cells were cultured in mTESR1 medium (STEMCELL Technologies, Vancouver, Canada) with daily media changes and passaged at 50 to 75% confluence. hiPSCs were differentiated into RPE following established protocols (*89*). Between days 50 and 90, RPE islands were isolated from surrounding cells using a 21-gauge needle based on characteristic cobblestone morphology and pigmentation. Mature cells were dissociated using 0.25% trypsin-EDTA solution (25200056, Gibco, Waltham, MA, USA), centrifuged, resuspended, and plated in transwells or plastic wells. They were gradually weaned off 10% FBS for a week, 3% FBS for another week, and 2% FBS for an additional week followed by maintenance in serum-free media. Cells were ready for experiments 6 weeks after plating in experimental vessels.

CGNP-IR775c labeling and cellular uptake

To label cells with CGNP-IR775c, cells were coincubated with CGNP-IR775c (50 μg/ml) for 24 hours (*19*, *90*). Labeled cells were washed with phosphate-buffered saline (PBS; 10010023, Gibco, Waltham, MA, USA) to remove excess serum and noninternalized CGNP-IR775c and then harvested and counted for subsequent viability assays and imaging analyses.

Moreover, to visualize intracellular uptake, cells (1×10^5 cells) were seeded in 35-mm culture dishes and treated with CGNP-IR775c as described above. Cells were counterstained with DAPI for nuclear visualization and imaged using an LSM 980 Airyscan 2 confocal laser scanning microscope (Zeiss, Oberkochen, Germany). DAPI-stained nuclei were excited at 405 nm, while cytoplasmic CGNP-IR775c was excited at 730 nm. Fluorescence signals from IR775c confirmed successful intracellular uptake. Fluorescent intensity was quantified using ZEN Microscopy software (Zeiss, Oberkochen, Germany).

Cytotoxicity assessment

The cytotoxicity of CGNP-IR775c was evaluated using 3-(4,5-dimethylthiazol-2-yl)−2,5-diphenyltetrazolium bromide (MTT) assay. Cells were treated with CGNP-IR775c at mass concentrations ranging from 50 to 500 μg/ml, seeded in 96-well plates, and incubated for 24 hours. Following incubation, cells were rinsed with PBS, and culture medium was replaced. Ten microliters of MTT (1117140001, Sigma-Aldrich, St. Louis, MO, USA) solution (5 mg/ml) was then added to each well and incubated for 4 hours. After media removal, formazan crystals were dissolved in 100 μl of dimethyl sulfoxide (D2653, Sigma-Aldrich, St. Louis, MO, USA). Absorbance at 570 nm was measured using a microplate reader spectrophotometer (Omega Plate Reader, BMG Labtech, Ortenberg, Germany), and viability was calculated as the ratio between the treatment and control groups.

Assessment of ROS sensitivity

The ROS responsiveness of CGNP-IR775c was evaluated using both acellular and cellular models. In the acellular model, solutions of CGNP (50 μg/ml), IR775c (50 μM), and CGNP-IR775c (50 μg/ml) were treated with H_2O_2 at concentrations ranging from 0 to 500 μM for 1 hour at room temperature. Optical property changes associated with ROS-induced degeneration were monitored using UV-Vis spectroscopy. For PA signal assessment, 20 μl of each H_2O_2-treated sample was loaded into silicone tubing (0.030″ ID × 0.065″ OD SILICONE

TUBING, Dow Corning, Midland, MI, USA), sealed to prevent leakage, and immersed in a water tank for acoustic coupling. PA imaging was performed at 620- and 775-nm wavelengths to capture ROS-dependent contrast changes.

In the cellular model, ARPE-19 and hiPSC-RPE cells were seeded at 1×10^5 cells per well and incubated with CGNP-IR775c (50 μg/ml) for 24 hours. To induce cell death and elevate intracellular ROS levels, cells were irradiated using a 532-nm photocoagulation laser (Vitra 532 nm, Quantel Medical, Cournon-d'Auvergne, France) at a power density of 150 mW/cm^2 for 5 min, delivering a total fluence of 45 J/cm^2. At 532 nm, laser energy is predominantly absorbed by melanin within RPE cells, choroid, and blood vessels and converted to heat, inducing thermal injury (*78*, *79*). Such photocoagulation-induced injury has been shown to elicit a mixed model cell death response, with necrosis predominating at early time points (~6 hours) and apoptosis becoming more prominent at later time points (~24 hours) (*80*), both of which are associated with elevated intracellular ROS production. Accordingly, this model was used to generate a ROS-rich cellular environment relevant for evaluating the responsiveness of CGNP-IR775c, rather than to isolate a single, defined cell death pathway. PA imaging was conducted at 620 and 775 nm using laser pulses with an energy of ~40 nJ, remaining within ANSI safety limits. This approach was chosen to closely mimic the intracellular oxidative stress environment rather than direct intervention of exogenous H_2O_2 treatment (*91*, *92*).

Laser-induced dead cells labeled with CGNP-IR775c were subjected to MTT assays to quantify cell viability. For fluorescence analysis, cells were counterstained with DAPI and imaged using confocal fluorescence microscopy (Zeiss, Oberkochen, Germany) to assess IR775c-associated fluorescence signal changes. Fluorescence intensity was quantified using ZEN Microscopy software (Zeiss, Oberkochen, Germany).

In vivo cell transplantation, cellular death induction, and multimodal imaging

All animal procedures were performed in compliance with the Association for Research in Vision and Ophthalmology statement for the Use of Animals in Ophthalmic and Vision Research and approved by the Institutional Animal Care and Use Committee at the University of Michigan (PRO00011327). Healthy New Zealand white rabbits (age: 2 to 6 months, weight: 2.6 to 3.2 kg, both genders, $N = 3$) were housed under controlled conditions (15° to 20°C, standard 12-hour light/dark cycle) with ad libitum access to food and water. Animals were obtained from the Center for Advanced Models and Translational Sciences and Therapeutics at the University of Michigan Medical School.

Before each experiment, and every 15 min after that, the heart rate, temperature, and respiratory rate of the animals were recorded and monitored using a pulse oximeter (V8400D Capnograph & SpO2 Digital Pulse Oximetry, Smiths Medical, MN, USA) until the rabbits were completely awake and ambulatory. Anesthesia was induced via intramuscular injection of ketamine (40 mg/kg) and xylazine (5 mg/kg). Pupil dilation was achieved using 1% tropicamide and 2.5% phenylephrine hydrochloride eye drops, followed by topical 0.5% proparacaine for local anesthesia. Animals were positioned supine under a surgical microscope. A 3-mm inferotemporal conjunctival peritomy was performed, and a subretinal injection site was marked 3.5 mm posterior to the limbus. Using a 25 G sterilized needle, ocular access was established while avoiding the lens, ciliary vasculature, and extraocular muscles. A contact lens and Gonak gel facilitated visualization of the ocular structures. In addition, during the experiment, a water circulating heating blanket was used to maintain a stable body temperature.

For cell transplantation, a suspension of CGNP-IR775c–labeled hiPSC-RPE cells (30 μl, 1×10^6 cells/ml) was loaded into a blunt 30 G Hamilton syringe and injected into the subretinal space via the vitreous. The injection targeted an area 0.5 to 1 optic disc diameter inferior to the retinal vessels. Slow injection created a localized subretinal bleb, indicating successful neurosensory retinal detachment. The syringe was retracted cautiously to prevent reflux.

To mitigate postoperative inflammation and immune-mediated rejection in this xenograft model, all animals received meloxicam (5 mg/ml, subcutaneous, once daily, for 3 days) and corticosteroid injections (triamcinolone, 40 mg/ml, intravitreal, once before transplantation, which provided 3 to 6 months of steroid immunosuppression locally) around the time of cell transplantation, maintained throughout the study period (*93*–*95*).

Four days posttransplantation, laser-induced cellular death was performed using a 532-nm photocoagulation laser (Vitra) delivered through a slit lamp (Carl Zeiss Meditec, Jena, Germany) to elevate local ROS levels and simulate graft stress in vivo. Laser irradiation was applied at a power of 100 mW with a 300-μm spot size and an exposure time of 1 s per shot. Multimodal imaging was performed using an integrated PAM and OCT system. Fundus photography was conducted using a Topcon 50EX system (Topcon Corporation, Tokyo, Japan) with an integrated EOS 5D camera (Canon, Tokyo, Japan). To monitor temporal dynamics following cell transplantation and laser-induced cellular death, multimodal imaging of rabbit eye was performed on day 0 (pretransplantation) and on days 4, 5, 6, 7, 9, 11, and 14 posttransplantation. All acquired images were processed using custom-developed MATLAB algorithms (MathWorks, Natick, MA, USA).

Histological analysis and TUNEL assay

We performed biosafety analysis to determine in vivo toxicity and validate the capability for monitoring cell viability. As a vital physiological indicator, the weight of the animals was measured every day during the study. Animals were euthanized by intravenous injection of sodium pentobarbital at a dose of 100 mg/kg and phenytoin (EUTHAPHEN, Dechra, Northwich, UK) at the experimental endpoint. Eyeballs were harvested after euthanasia and preserved for 24 hours in Davidson's fixative solution (Thermo Fisher Scientific, Waltham, MA, USA). They were then immersed in 50% alcohol for 8 hours and 70% alcohol for another 24 hours before being sectioned. For histological examination, the samples were cut in half, immersed in paraffin, and then sectioned into 4- to 6-μm slices.

Tissue morphology and structural integrity were assessed by H&E staining. TUNEL assays were performed using the in situ apoptosis detection kit protocol (Novus Biologicals, Centennial, CO, USA) to evaluate the biological impact of CGNP-IR775c–labeled hiPSC-RPE cell transplantation and assess local tissue response and stem cell viability in vivo. All stained H&E and TUNEL samples were examined using a DM6000 microscope (Leica Microsystems, Wetzlar, Germany).

Quantitative analysis of TUNEL positivity was performed using open-source software ImageJ/FIJI. For each tissue section, five non-overlapping fields of view were analyzed per region (laser-irradiated and nonirradiated). Regions of interest (ROIs) were defined on the basis of anatomical boundaries identified by cross-referencing with

H&E-stained sections and were restricted to DAPI-positive nucleated cells within the transplanted cell region, explicitly excluding the choroidal layer and photoreceptor outer segments. Total nuclei were counted in the DAPI channel and TUNEL-positive nuclei in the green channel using automated thresholding (Otsu method) followed by Watershed segmentation and particle analysis. TUNEL positivity rate was calculated as the percentage of TUNEL and DAPI double-positive cells relative to total DAPI-positive cells per region.

Statistical analysis

Statistical analysis was performed with GraphPad Prism 10 (GraphPad Software Inc., San Diego, CA, USA). Data are shown as mean ± SD of three independent experiments unless otherwise specified. Data distribution normality was evaluated by applying the Shapiro-Wilk test. For comparisons between groups with normally distributed but unequal variances, the Welch's t test was applied. For nonnormally distributed independent samples, the Mann-Whitney U test was used. A paired t test was used to assess paired samples with normal distribution. Statistical significance was defined as $P < 0.05$, with significance levels indicated as not significant ($P > 0.05$), $*P \leq 0.05$, $**P \leq 0.01$, $***P \leq 0.001$, and $****P \leq 0.0001$. No data were excluded from the analyses.

Supplementary Materials

This PDF file includes:

Figs. S1 to S7

REFERENCES

1. Y. Niu, J. Ji, K. Yao, Q. Fu, Regenerative treatment of ophthalmic diseases with stem cells: Principles, progress, and challenges. *Adv. Ophthalmol. Pract. Res.* **4**, 52–64 (2024).
2. I. W. Caras, L. R. Collins, A. A. Creasey, A stem cell journey in ophthalmology: From the bench to the clinic. *Stem Cells Transl. Med.* **10**, 1581–1587 (2021).
3. G. Miotti, P. C. Parodi, M. Zeppieri, Stem cell therapy in ocular pathologies in the past 20 years. *World J. Stem Cells* **13**, 366–385 (2021).
4. C. A. Herberts, M. S. Kwa, H. P. Hermsen, Risk factors in the development of stem cell therapy. *J. Transl. Med.* **9**, 29 (2011).
5. C. A. P. Vilela, A. Messias, R. T. Calado, R. C. Siqueira, M. J. L. Silva, D. T. Covas, J. S. Paula, Retinal function after intravitreal injection of autologous bone marrow-derived mesenchymal stromal cells in advanced glaucoma. *Doc. Ophthalmol.* **143**, 33–38 (2021).
6. S. Cell, Stem Cells: A Comprehensive Guide to Origins, Functions, and Mechanisms, *Stem Cells: A Comprehensive Guide to Origins, Functions, and Mechanisms* (2024); https://drstemcell.com/blog/stem-cells-a-comprehensive-guide-to-origins-functions-and-mechanisms.
7. S. Baldari, G. Di Rocco, M. Piccoli, M. Pozzobon, M. Muraca, G. Toietta, Challenges and strategies for improving the regenerative effects of mesenchymal stromal cell-based therapies. *Int. J. Mol. Sci.* **18**, 2087 (2017).
8. L. Wei, W. Yan, W. Shah, Z. Zhang, M. Wang, B. Liu, Z. Xue, Y. Cao, X. Hou, K. Zhang, B. Yan, X. Wang, Advancements and challenges in stem cell transplantation for regenerative medicine. *Heliyon* **10**, e35836 (2024).
9. A. Ripolles-Garcia, N. Dolgova, M. J. Phillips, S. Savina, A. L. Ludwig, S. A. Stuedemann, U. Nlebedum, J. H. Wolfe, O. A. Garden, A. Maminishkis, J. Amaral, K. Bharti, D. M. Gamm, G. D. Aguirre, W. A. Beltran, Systemic immunosuppression promotes survival and integration of subretinally implanted human ESC-derived photoreceptor precursors in dogs. *Stem Cell Rep.* **17**, 1824–1841 (2022).
10. A. N. Dunuweera, S. P. Dunuweera, K. Ranganathan, A comprehensive exploration of bioluminescence systems, mechanisms, and advanced assays for versatile applications. *Biochem. Res. Int.* **2024**, 8273237 (2024).
11. A. Refaat, M. L. Yap, G. Pietersz, A. P. G. Walsh, J. Zeller, B. del Rosal, X. Wang, K. Peter, In vivo fluorescence imaging: Success in preclinical imaging paves the way for clinical applications. *J. Nanobiotechnology* **20**, 450 (2022).
12. W. Zhang, Y. Li, V. P. Nguyen, Z. Huang, Z. Liu, X. Wang, Y. M. Paulus, High-resolution, in vivo multimodal photoacoustic microscopy, optical coherence tomography, and fluorescence microscopy imaging of rabbit retinal neovascularization. *Light Sci. Appl.* **7**, 103 (2018).
13. M. Zheng, Y. M. Paulus, M. Zheng, Y. M. Paulus, Multimodal imaging in stem cell therapy for retinal disease. *Photonics* **12**, 413 (2025).
14. C. Tian, W. Zhang, A. Mordovanakis, X. Wang, Y. M. Paulus, Noninvasive chorioretinal imaging in living rabbits using integrated photoacoustic microscopy and optical coherence tomography. *Opt. Express* **25**, 15947–15955 (2017).
15. Y. Li, W. Zhang, V. P. Nguyen, N. W. Khan, X. Xia, X. Wang, Y. M. Paulus, Retinal safety evaluation of photoacoustic microscopy. *Exp. Eye Res.* **202**, 108368 (2021).
16. W. Zhang, Y. Li, V. P. Nguyen, K. Derouin, X. Xia, Y. M. Paulus, X. Wang, Ultralow energy photoacoustic microscopy for ocular imaging in vivo. *J. Biomed. Opt.* **25**, 066003 (2020).
17. K. P. Kubelick, E. J. Snider, C. R. Ethier, S. Emelianov, Development of a stem cell tracking platform for ophthalmic applications using ultrasound and photoacoustic imaging. *Theranostics* **9**, 3812–3824 (2019).
18. V. P. Nguyen, W. Fan, T. Zhu, W. Qian, Y. Li, B. Liu, W. Zhang, J. Henry, S. Yuan, X. Wang, Y. M. Paulus, Long-term, noninvasive in vivo tracking of progenitor cells using multimodality photoacoustic, optical coherence tomography, and fluorescence imaging. *ACS Nano* **15**, 13289–13306 (2021).
19. V. P. Nguyen, A. J. Karoukis, W. Qian, L. Chen, N. D. Perera, D. Yang, Q. Zhang, J. Zhe, J. Henry, B. Liu, W. Zhang, A. T. Fahim, X. Wang, Y. M. Paulus, Multimodal imaging-guided stem cell ocular treatment. *ACS Nano* **18**, 14893–14906 (2024).
20. K. S. Dhada, D. S. Hernandez, L. J. Suggs, In vivo photoacoustic tracking of mesenchymal stem cell viability. *ACS Nano* **13**, 7791–7799 (2019).
21. M. Redza-Dutordoir, D. A. Averill-Bates, Activation of apoptosis signalling pathways by reactive oxygen species. *Biochim. Biophys. Acta Mol. Cell Res.* **1863**, 2977–2992 (2016).
22. M. L. Circu, T. Y. Aw, Reactive oxygen species, cellular redox systems and apoptosis. *Free Radic. Biol. Med.* **48**, 749–762 (2010).
23. M. Li, Y. Song, N. Song, G. Wu, H. Zhou, J. Long, P. Zhang, L. Shi, Z. Yu, Supramolecular antagonists promote mitochondrial dysfunction. *Nano Lett.* **21**, 5730–5737 (2021).
24. S. Kuang, L. Sun, X. Zhang, X. Liao, T. W. Rees, L. Zeng, Y. Chen, X. Zhang, L. Ji, H. Chao, A mitochondrion-localized two-photon photosensitizer generating carbon radicals against hypoxic tumors. *Angew. Chem. Int. Ed. Engl.* **59**, 20697–20703 (2020).
25. T. Zhou, J. Zheng, H. Cao, X. Wang, K. Lou, X. Zhang, Y. Tao, Growth suppression and apoptosis-like cell death in *Microcystis aeruginosa* by H2O2: A new insight into extracellular and intracellular damage pathways. *Chemosphere* **211**, 1098–1108 (2018).
26. P. Mikula, S. Zezulka, D. Jancula, B. Marsalek, Metabolic activity and membrane integrity changes in *Microcystis aeruginosa*–New findings on hydrogen peroxide toxicity in cyanobacteria. *Eur. J. Phycol.* **47**, 195–206 (2012).
27. E. Giampazolias, B. Zunino, S. Dhayade, F. Bock, C. Cloix, K. Cao, A. Roca, J. Lopez, G. Ichim, E. Proïcs, C. Rubio-Patiño, L. Fort, N. Yatim, E. Woodham, S. Orozco, L. Taraborrelli, N. Peltzer, D. Lecis, L. Machesky, H. Walczak, M. L. Albert, S. Milling, A. Oberst, J.-E. Ricci, K. M. Ryan, K. Blyth, S. W. G. Tait, Mitochondrial permeabilization engages NF-κB-dependent anti-tumour activity under caspase deficiency. *Nat. Cell Biol.* **19**, 1116–1129 (2017).
28. M. Zhang, N. Harashima, T. Moritani, W. Huang, M. Harada, The roles of ROS and caspases in TRAIL-induced apoptosis and necroptosis in human pancreatic cancer cells. *PLOS ONE* **10**, e0127386 (2015).
29. D. Bertheloot, E. Latz, B. S. Franklin, Necroptosis, pyroptosis and apoptosis: An intricate game of cell death. *Cell. Mol. Immunol.* **18**, 1106–1121 (2021).
30. D. A. Ammendolia, W. M. Bement, J. H. Brumell, Plasma membrane integrity: Implications for health and disease. *BMC Biol.* **19**, 71 (2021).
31. N. Liao, L. Su, Y. Cao, L. Qiu, R. Xie, F. Peng, Z. Cai, X. Liu, J. Song, Y. Zeng, Tracking cell viability for adipose-derived mesenchymal stem cell-based therapy by quantitative fluorescence imaging in the second near-infrared window. *ACS Nano* **16**, 2889–2900 (2022).
32. C. Yang, J. Yang, A. Lu, J. Gong, Y. Yang, X. Lin, M. Li, H. Xu, Nanoparticles in ocular applications and their potential toxicity. *Front. Mol. Biosci.* **9**, 931759 (2022).
33. J. S. Suk, Q. Xu, N. Kim, J. Hanes, L. M. Ensign, PEGylation as a strategy for improving nanoparticle-based drug and gene delivery. *Adv. Drug Deliv. Rev.* **99**, 28–51 (2016).
34. I. Ozcicek, N. Aysit, C. Cakici, A. Aydeger, The effects of surface functionality and size of gold nanoparticles on neuronal toxicity, apoptosis, ROS production and cellular/suborgan biodistribution. *Mater. Sci. Eng. C* **128**, 112308 (2021).
35. D. Prakashan, N. S. Shrikrishna, M. Byakodi, K. Nagamani, S. Gandhi, Gold nanoparticle conjugate-based lateral flow immunoassay (LFIA) for rapid detection of RBD antigen of SARS-CoV-2 in clinical samples using a smartphone-based application. *J. Med. Virol.* **95**, e28416 (2023).
36. M. Li, Y. Tang, J. Yao, Photoacoustic tomography of blood oxygenation: A mini review. *Photoacoustics* **10**, 65–73 (2018).
37. L. Zhang, H. Jia, X. Liu, Y. Zou, J. Sun, M. Liu, S. Jia, N. Liu, Y. Li, Q. Wang, Heptamethine cyanine–based application for cancer theranostics. *Front. Pharmacol.* **12**, 764654 (2022).
38. T. Duong, X. Li, B. Yang, C. Schumann, H. A. Albarqi, O. Taratula, O. Taratula, Phototheranostic nanoplatform based on a single cyanine dye for image-guided combinatorial phototherapy. *Nanomedicine Nanotechnol. Biol. Med.* **13**, 955–963 (2017).
39. H. Mustroph, Bring back order in the polymethine dye medley: Classification, structure and spectra. *Dyes Pigments* **208**, 110783 (2023).

40. C. Zhang, X. Wang, J. Du, Z. Gu, Y. Zhao, Reactive oxygen species-regulating strategies based on nanomaterials for disease treatment. *Adv. Sci.* **8**, 2002797 (2021).
41. J. D. Clogston, A. K. Patri, "Zeta potential measurement," in *Characterization of Nanoparticles Intended for Drug Delivery*, S. E. McNeil, Ed. (Humana Press, 2011), pp. 63–70; https://doi.org/10.1007/978-1-60327-198-1_6.
42. M. Ramzan, M. Rani, R. Siddiqui, A. Ahmad Shah, M. Arshad, M. W. Ghauri, G. Abbas, K. Yusuf, M. Sillanpää, Synthesis and analytical characterization of Ca-BTC metal organic framework. *Heliyon* **9**, e21314 (2023).
43. J. D. Clogston, A. Vermilya, "Measuring zeta potential of nanoparticles: Version 1.2," in *National Cancer Institute's Nanotechnology Characterization Laboratory Assay Cascade Protocols* [National Cancer Institute (US), 2005]; http://ncbi.nlm.nih.gov/books/NBK604914/.
44. I. Ostolska, M. Wiśniewska, Application of the zeta potential measurements to explanation of colloidal Cr_2O_3 stability mechanism in the presence of the ionic polyamino acids. *Colloid Polym. Sci.* **292**, 2453–2464 (2014).
45. A. Troyano, P. Sancho, C. Fernández, E. de Blas, P. Bernardi, P. Aller, The selection between apoptosis and necrosis is differentially regulated in hydrogen peroxide-treated and glutathione-depleted human promonocytic cells. *Cell Death Differ.* **10**, 889–898 (2003).
46. A. Davies, T. Pottage, A. Bennett, J. Walker, Gaseous and air decontamination technologies for *Clostridium difficile* in the healthcare environment. *J. Hosp. Infect.* **77**, 199–203 (2011).
47. Y. Tian, S. Liu, W. Cao, P. Wu, Z. Chen, H. Xiong, H2O2-activated NIR-II fluorescent probe with a large stokes shift for high-contrast imaging in drug-induced liver injury mice. *Anal. Chem.* **94**, 11321–11328 (2022).
48. J. Chen, L. Chen, Y. Wu, Y. Fang, F. Zeng, S. Wu, Y. Zhao, A H2O2-activatable nanoprobe for diagnosing interstitial cystitis and liver ischemia-reperfusion injury via multispectral optoacoustic tomography and NIR-II fluorescent imaging. *Nat. Commun.* **12**, 6870 (2021).
49. S. Rosa, C. Connolly, G. Schettino, K. T. Butterworth, K. M. Prise, Biological mechanisms of gold nanoparticle radiosensitization. *Cancer Nanotechnol.* **8**, 2 (2017).
50. Z. Zhang, A. Berg, H. Levanon, R. W. Fessenden, D. Meisel, On the interactions of free radicals with gold nanoparticles. *J. Am. Chem. Soc.* **125**, 7959–7963 (2003).
51. Y. Hong, A. Boiti, D. Vallone, N. S. Foulkes, Reactive oxygen species signaling and oxidative stress: Transcriptional regulation and evolution. *Antioxidants* **13**, 312 (2024).
52. T. Konno, E. P. Melo, J. E. Chambers, E. Avezov, Intracellular sources of ROS/H_2O_2 in health and neurodegeneration: Spotlight on endoplasmic reticulum. *Cells* **10**, 233 (2021).
53. S. A. Sinenko, T. Y. Starkova, A. A. Kuzmin, A. N. Tomilin, Physiological signaling functions of reactive oxygen species in stem cells: From flies to man. *Front. Cell Dev. Biol.* **9**, 714370 (2021).
54. A. J. P. O. de Almeida, J. C. P. L. de Oliveira, L. V. da Silva Pontes, J. F. de Souza Júnior, T. A. F. Gonçalves, S. H. Dantas, M. S. de Almeida Feitosa, A. O. Silva, I. A. de Medeiros, ROS: Basic concepts, sources, cellular signaling, and its implications in aging pathways. *Oxid. Med. Cell. Longev.* **2022**, 1225578 (2022).
55. A. M. Alkilany, C. J. Murphy, Toxicity and cellular uptake of gold nanoparticles: What we have learned so far? *J. Nanoparticle Res.* **12**, 2313–2333 (2010).
56. E. Canepa, S. Salassi, F. Simonelli, R. Ferrando, R. Rolandi, C. Lambruschini, F. Canepa, S. Dante, A. Relini, G. Rossi, Non-disruptive uptake of anionic and cationic gold nanoparticles in neutral zwitterionic membranes. *Sci. Rep.* **11**, 1256 (2021).
57. R. Augustine, A. Hasan, R. Primavera, R. J. Wilson, A. S. Thakor, B. D. Kevadiya, Cellular uptake and retention of nanoparticles: Insights on particle properties and interaction with cellular components. *Mater. Today Commun.* **25**, 101692 (2020).
58. J. Yue, T. J. Feliciano, W. Li, A. Lee, T. W. Odom, Gold nanoparticle size and shape effects on cellular uptake and intracellular distribution of siRNA nanoconstructs. *Bioconjug. Chem.* **28**, 1791–1800 (2017).
59. P. H. Hemmerich, A. H. von Mikecz, Defining the subcellular interface of nanoparticles by live-cell imaging. *PLOS ONE* **8**, e62018 (2013).
60. M. Aoyama, Y. Yoshioka, Y. Arai, H. Hirai, R. Ishimoto, K. Nagano, K. Higashisaka, T. Nagai, Y. Tsutsumi, Intracellular trafficking of particles inside endosomal vesicles is regulated by particle size. *J. Controlled Release* **260**, 183–193 (2017).
61. C. M. C. Andrés, J. M. Pérez de la Lastra, C. A. Juan, F. J. Plou, E. Pérez-Lebeña, Chemistry of hydrogen peroxide formation and elimination in mammalian cells, and its role in various pathologies. *Stresses* **2**, 256–274 (2022).
62. G. P. Bienert, F. Chaumont, Aquaporin-facilitated transmembrane diffusion of hydrogen peroxide. *Biochim. Biophys. Acta Gen. Subj.* **1840**, 1596–1604 (2014).
63. J. R. Treberg, Review: Using isolated mitochondria to investigate mitochondrial hydrogen peroxide metabolism. *Comp. Biochem. Physiol. B Biochem. Mol. Biol.* **256**, 110614 (2021).
64. A. Laporte, S. Lortz, C. Schaal, S. Lenzen, M. Elsner, Hydrogen peroxide permeability of cellular membranes in insulin-producing cells. *Biochim. Biophys. Acta Biomembr.* **1862**, 183096 (2020).
65. V. P. Nguyen, W. Qian, Y. Li, B. Liu, M. Aaberg, J. Henry, W. Zhang, X. Wang, Y. M. Paulus, Chain-like gold nanoparticle clusters for multimodal photoacoustic microscopy and optical coherence tomography enhanced molecular imaging. *Nat. Commun.* **12**, 34 (2021).
66. S. Wang, S. Guo, J. Guo, Q. Du, C. Wu, Y. Wu, Y. Zhang, Cell death pathways: Molecular mechanisms and therapeutic targets for cancer. *MedComm* **5**, e693 (2024).
67. S. Shen, Y. Shao, C. Li, Different types of cell death and their shift in shaping disease. *Cell Death Discov.* **9**, 284 (2023).
68. Z. Darzynkiewicz, D. Galkowski, H. Zhao, Analysis of apoptosis by cytometry using TUNEL assay. *Methods* **44**, 250–254 (2008).
69. S. Lee, E. Choi, M.-J. Cha, K.-C. Hwang, Cell adhesion and long-term survival of transplanted mesenchymal stem cells: A prerequisite for cell therapy. *Oxid. Med. Cell. Longev.* **2015**, 632902 (2015).
70. S. Petrus-Reurer, M. Romano, S. Howlett, J. L. Jones, G. Lombardi, K. Saeb-Parsy, Immunological considerations and challenges for regenerative cellular therapies. *Commun. Biol.* **4**, 798 (2021).
71. N. Azene, Y. Fu, J. Maurer, D. L. Kraitchman, Tracking of stem cells in vivo for cardiovascular applications. *J. Cardiovasc. Magn. Reson.* **16**, 7 (2014).
72. J. Wang, Q. Li, W. Li, N. Méndez-Sánchez, X. Liu, X. Qi, J. Wang, Q. Li, W. Li, N. Méndez-Sánchez, X. Liu, X. Qi, Stem cell therapy for liver diseases: Current perspectives. *Front. Biosci. Landmark* **28**, 359 (2023).
73. Y. Zheng, J. Huang, T. Zhu, R. Li, Z. Wang, F. Ma, J. Zhu, Stem cell tracking technologies for neurological regenerative medicine purposes. *Stem Cells Int.* **2017**, 2934149 (2017).
74. S. Quellmann, G. Schwarzer, K. Hübel, A. Greb, A. Engert, J. Bohlius, Corticosteroids for preventing graft-versus-host disease after allogeneic myeloablative stem cell transplantation. *Cochrane Database Syst. Rev.* **2008**, CD004885 (2008).
75. R.-J. Swijnenburg, S. Schrepfer, J. A. Govaert, F. Cao, K. Ransohoff, A. Y. Sheikh, M. Haddad, A. J. Connolly, M. M. Davis, R. C. Robbins, J. C. Wu, Immunosuppressive therapy mitigates immunological rejection of human embryonic stem cell xenografts. *Proc. Natl. Acad. Sci. U.S.A.* **105**, 12991–12996 (2008).
76. J. Scalea, I. Hanecamp, S. C. Robson, K. Yamada, T-cell-mediated immunological barriers to xenotransplantation. *Xenotransplantation* **19**, 23–30 (2012).
77. A. Dorling, R. I. Lechler, T cell-mediated xenograft rejection: Specific tolerance is probably required for long term xenograft survival. *Xenotransplantation* **5**, 234–245 (1998).
78. S. Sivaprasad, M. Elagouz, D. McHugh, O. Shona, G. Dorin, Micropulsed diode laser therapy: Evolution and clinical applications. *Surv. Ophthalmol.* **55**, 516–530 (2010).
79. D. Lavinsky, J. Wang, P. Huie, R. Dalal, S. J. Lee, D. Y. Lee, D. Palanker, Nondamaging retinal laser therapy: rationale and applications to the macula. *Invest. Ophthalmol. Vis. Sci.* **57**, 2488–2500 (2016).
80. P. Tababat-Khani, L. M. Berglund, C.-D. Agardh, M. F. Gomez, E. Agardh, Photocoagulation of human retinal pigment epithelial cells in vitro: Evaluation of necrosis, apoptosis, cell migration, cell proliferation and expression of tissue repairing and cytoprotective genes. *PLOS ONE* **8**, e70465 (2013).
81. N. Sendtner, R. Seitz, N. Brandl, M. Müller, K. Gülow, Reactive oxygen species across death pathways: Gatekeepers of apoptosis, ferroptosis, pyroptosis, paraptosis, and beyond. *Int. J. Mol. Sci.* **26**, 10240 (2025).
82. J. Hanus, H. Zhang, Z. Wang, Q. Liu, Q. Zhou, S. Wang, Induction of necrotic cell death by oxidative stress in retinal pigment epithelial cells. *Cell Death Dis.* **4**, e965 (2013).
83. A. P. Gorka, M. J. Schnermann, Harnessing cyanine photooxidation: From slowing photobleaching to near-IR uncaging. *Curr. Opin. Chem. Biol.* **33**, 117–125 (2016).
84. V. P. Nguyen, W. Qian, J. Zhe, J. Henry, M. Wang, B. Liu, W. Zhang, X. Wang, Y. M. Paulus, Renally clearable ultraminiature chain-like gold nanoparticle clusters for multimodal molecular imaging of choroidal neovascularization. *Adv. Mater.* **35**, e2302069 (2023).
85. P. Hajireza, A. Forbrich, R. J. Zemp, Multifocus optical-resolution photoacoustic microscopy using stimulated Raman scattering and chromatic aberration. *Opt. Lett.* **38**, 2711–2713 (2013).
86. P. Hajireza, A. Forbrich, R. Zemp, In-vivo functional optical-resolution photoacoustic microscopy with stimulated Raman scattering fiber-laser source. *Biomed. Opt. Express* **5**, 539–546 (2014).
87. K. Okamoto, "Chapter 5—Nonlinear optical effects in optical fibers," in *Fundamentals of Optical Waveguides*, K. Okamoto, Ed. (Academic Press, ed. 2, 2006), pp. 209–259; https://sciencedirect.com/science/article/pii/B9780125250962500064.
88. W. Qian, M. Murakami, Y. Ichikawa, Y. Che, Highly efficient and controllable PEGylation of gold nanoparticles prepared by femtosecond laser ablation in water. *J. Phys. Chem. C* **115**, 23293–23298 (2011).
89. G. Fanelli, A. Gonzalez-Cordero, P. J. Gardner, Q. Peng, M. Fernando, M. Kloc, C. A. Farrar, A. Naeem, P. Garred, R. R. Ali, S. H. Sacks, Human stem cell-derived retinal epithelial cells activate complement via collectin 11 in response to stress. *Sci. Rep.* **7**, 14625 (2017).
90. P. Van Nguyen, W. Fan, T. Zhu, W. Qian, Y. Li, B. Liu, W. Zhang, J. Henry, S. Yuan, X. Wang, Y. M. Paulus, Long-term, non-invasive in vivo tracking of progenitor cells using

multimodality photoacoustic, optical coherence tomography, and fluorescence imaging. *ACS Nano* **15**, 13289–13306 (2021).
91. S. Wu, D. Xing, X. Gao, W. R. Chen, High fluence low-power laser irradiation induces mitochondrial permeability transition mediated by reactive oxygen species. *J. Cell. Physiol.* **218**, 603–611 (2009).
92. S. Wu, X. Da, F. Wang, T. Chen, W. R. Chen, Mechanistic study of apoptosis induced by high-fluence low-power laser irradiation using fluorescence imaging techniques. *J. Biomed. Opt.* **12**, 064015 (2007).
93. A. Plaza Reyes, S. Petrus-Reurer, L. Antonsson, S. Stenfelt, H. Bartuma, S. Panula, T. Mader, I. Douagi, H. André, O. Hovatta, F. Lanner, A. Kvanta, Xeno-free and defined human embryonic stem cell-derived retinal pigment epithelial cells functionally integrate in a large-eyed preclinical model. *Stem Cell Rep.* **6**, 9–17 (2015).
94. S. Petrus-Reurer, H. Bartuma, M. Aronsson, S. Westman, F. Lanner, H. André, A. Kvanta, Integration of subretinal suspension transplants of human embryonic stem cell-derived retinal pigment epithelial cells in a large-eyed model of geographic atrophy. *Invest. Ophthalmol. Vis. Sci.* **58**, 1314–1322 (2017).
95. V. P. Nguyen, Y. Li, J. Henry, T. Qian, W. Zhang, X. Wang, Y. M. Paulus, In vivo subretinal ARPE-19 cell tracking using indocyanine green contrast-enhanced multimodality photoacoustic microscopy, optical coherence tomography, and fluorescence imaging for regenerative medicine. *Transl. Vis. Sci. Technol.* **10**, 10 (2021).

Acknowledgments
Funding: This research was supported by the National Institutes of Health under the grant number of R01EY034325 (Y.M.P. and X.W.), 1R01EY033000 (Y.M.P.), as well as the Core Center for Vision Research, funded by the National Eye Institute (P30 EY007003) (Y.M.P), Fight for Sight-International Retinal Research Foundation (FFSGIA16002) (Y.M.P.), Alcon Research Institute Young Investigator Grant (Y.M.P.), unrestricted departmental funding from Research to Prevent Blindness (Y.M.P.), and the Dr. Jonas Friedenwald Professorship in Ophthalmology (Y.M.P.). **Author contributions:** Conceptualization: S.P., Y.M.P., and X.W. Methodology: S.P., W.Q., J.F., V.P.N., N.D.P., and W.Z. Investigation: S.P., W.Q., J.F., V.P.N., N.D.P., and W.Z. Visualization: S.P., W.Q., J.F., N.D.P., and W.Z. Resources: A.T.F., Y.M.P., and X.W. Funding acquisition: Y.M.P. and X.W. Supervision: Y.M.P. and X.W. Writing—original draft: S.P., W.Q., and J.F. Writing—review and editing: S.P., W.Q., J.F., V.P.N., N.D.P., A.T.F., Y.M.P., and X.W. **Competing interests:** The authors declare that they have no competing interests. **Data, code, and materials availability:** All data and code needed to evaluate and reproduce the results in the paper are present in the paper and/or the Supplementary Materials. This study did not generate new materials.

Submitted 21 April 2026
Accepted 15 October 2026
Published 20 November 2026
10.1126/sciadv.aei1820